

Confined Vortex Surface and Irreversibility. 2. Exact Solutions and Turbulent Statistics

Alexander Migdal

*Abu Dhabi Investment Authority, 211 Corniche Street,
Abu Dhabi, United Arab Emirates*

*Department of Physics, New York University Abu Dhabi, PO Box 129188,
Saadiyat Island, Abu Dhabi, United Arab Emirates*

We continue the study of Confined Vortex Surfaces (CVS) that we introduced in the previous paper. We classify exact solutions of the CVS equation and find finite closed loops in the cross-section of the cylindrical tube. We find the corresponding velocity field inside and outside the tube as a parametric equation involving hypergeometric functions.

We use the dilute gas approximation for the vorticity structures in a turbulent flow, assuming their size is much smaller than the mean distance between them.

We introduce the Gaussian random background strain for each vortex surface as an accumulation of a large number of small random contributions coming from other surfaces far away. We compute this self-consistent background strain, relating the variance of the strain to the energy dissipation rate.

This random matrix theory applied to the cylindrical solution leads to a universal asymmetric distribution for the tube cross-section at fixed energy dissipation.

The fluctuations of the tube size naturally lead to something similar to multifractal scaling of the moments of velocity difference $v(\vec{r}_1) - v(\vec{r}_2)$. More precisely, these moments have a nontrivial dependence of $n, \log|r_1 - r_2|$, which one can approximate as a power law with nonlinear index $\zeta(n)$. We argue that the approximate relations for these moments suggested in a recent paper by Sreenivasan and Yakhot are consistent with the CVS theory. We reinterpret their renormalization parameter $\alpha \approx 0.95$ in the Bernoulli law $p = -\frac{1}{2}\alpha\bar{v}^2$ as a probability to find no vortex surface at a random point in space. Numerical computation of multidimensional integrals involved in our formulas for velocity moments and comparison with the DNS we leave for future study.

1. Introduction

The ultimate goal of turbulence studies is to solve the Navier-Stokes equations and determine why and how the solution covers some manifold rather than staying unique given initial data and boundary conditions.

We also need to understand why it is irreversible even in the limit of zero viscosity when the Navier-Stokes equations formally become the Euler equation corresponding to the reversible Hamiltonian system with conserved energy.

Once we know why and how the solution covers some manifold – a degenerate fixed point of the Navier-Stokes equations – we would like to know the parameters and the invariant measure on this manifold.

The first obstacle to overcome on this path is to understand the irreversibility

of the Navier-Stokes dynamics in a limit when the viscosity goes to zero at fixed energy dissipation.

We know (or at least we assume) that the vortex structures in this extreme turbulent flow collapse into thin clusters in physical space. Snapshots of vorticity in numerical simulations^{1,2} show a collection of tube-like structures relatively sparsely distributed in space.

There was an excellent recent DNS³ studying statistics of vorticity structures in isotropic turbulence with a high Reynolds number. The distribution of velocity circulation they have found was compatible with 2D vortex structures (instantons) suggested in⁴ following our early suggestions about area law for the velocity circulation.⁵

There were also some recent works modeling sparse vortex structures in classical,⁶ and quantum⁷ turbulence.

We know such 2D structures in the Euler dynamics: these are vortex surfaces. Vorticity collapses into a thin boundary layer around the surface which is moving in a self-generated velocity field. Such motion is known to be unstable against the Kelvin-Helmholtz instabilities, which undermines the whole idea of random vortex surfaces.

However, the exact solutions of the Navier-Stokes equations discovered in the previous century by Burgers and Townsend^{8,9} show stable planar sheets with Gaussian profile of the vorticity in the normal direction.

Thus, the viscosity effects in certain cases suppress the Kelvin-Helmholtz instabilities leading to stable, steady vortex structures.

This stable Gaussian solution is not the most general one; it takes some tuning of parameters in the background flow. This tuning is the central subject of our previous paper¹⁰ as well as this one.

Let us define the conditions and assumptions we presume in this paper as well as the previous one.

- (1) We address the turbulence problem from the first principle, the Navier-Stokes equation without external forcing.
- (2) We study an infinite isotropic flow in the extreme turbulent limit (viscosity going to zero at fixed anomalous dissipation rate).
- (3) The flow is assumed to be potential everywhere except narrow boundary layers surrounding closed vortex surfaces (shaped as tubes).
- (4) We restrict ourselves to the steady solutions (fixed points of Euler equations) and investigate the stability of these fixed points, leading to new boundary conditions of the Euler equations on vortex surfaces.
- (5) As we shall argue, the effective internal forcing (spontaneous stochasticity) is generated by the infinite number of randomly located remote vortex structures, leading to a Gaussian random strain tensor.
- (6) This Gaussian random matrix parametrizes our fixed point manifold, leading to a calculable probability distribution.

The recent research^{11,12} revealed that the Burgers-Townsend regime required certain restrictions on the eigenvalues of the background strain for the planar vortex sheet solution.

Abstracting from these observations, we conjectured¹⁰ that the local stability condition of the vortex surface with the local normal vector $\vec{\sigma}$ and local mean boundary value of the strain tensor S reduces to three equations (with \vec{v}_{\pm} being the boundary values of velocity on each side)

$$\vec{v}_{\pm} \cdot \vec{\sigma} = 0; \quad (1)$$

$$\hat{S} \cdot (\vec{v}_+ - \vec{v}_-) = 0; \quad (2)$$

$$S_{nn} = \vec{\sigma} \cdot \hat{S} \cdot \vec{\sigma} < 0 \quad (3)$$

We call these equations the Confined Vortex Surface or *CVS* equations. They are supposed to hold at every point of the vortex surface, thus imposing extra boundary conditions on the Euler equations.

As the local strain tensor for the fixed vortex surface is uniquely determined by conventional Neumann boundary conditions for potential flow on each side, these additional *CVS* boundary conditions restrict allowed shapes of vortex surfaces.

The first *CVS* equation is simply a statement that the surface is stationary. The second one is an enhanced version of the vanishing eigenvalue requirement. The velocity gap $\Delta\vec{v} = \vec{v}_+ - \vec{v}_-$ should be a null vector for this zero eigenvalue. This requirement is stronger than $\det \hat{S} = 0$.

The third equation demands that the strain pushes the fluid towards the surface on both sides.

With negative normal strain and zero strain in the direction of velocity gap, the flow effortlessly slides along the surface on both sides, without leakage and pile-up.

Here is an intuitive explanation of the *CVS* conditions– they provide the permanent tangential flow around the surface, confining vorticity inside the boundary layer.

Once these requirements are satisfied in the local tangent plane, one could solve the Navier-Stokes equation in the (flat) boundary layer and obtain the Gaussian Burgers-Townsend solution, vindicating the stability hypothesis. The error function of the normal coordinate will replace the velocity gap, and the delta function of tangent vorticity will become the Gaussian profile with viscous width.

The flow in the boundary layer surrounding the local tangent plane has the

form¹³ (with $\Phi_{\pm}(r)$ being velocity potentials on both sides)

$$\vec{v}(\vec{r}_0 + \vec{\sigma}_0 \zeta) = \frac{1}{2}(\vec{v}_+(\vec{r}_0) + \vec{v}_-(\vec{r}_0)) + \frac{1}{2}(\vec{v}_+(\vec{r}_0) - \vec{v}_-(\vec{r}_0)) \operatorname{erf}\left(\frac{\zeta}{h\sqrt{2}}\right); \quad (4)$$

$$\vec{\sigma}_0 = \vec{\sigma}(\vec{r}_0); \quad (5)$$

$$\vec{v}_{\pm}(\vec{r}_0) = \vec{\nabla}\Phi_{\pm}(\vec{r}_0); \quad (6)$$

$$\vec{\omega}(\vec{r}_0 + \vec{\sigma}_0 \zeta) = \frac{\sqrt{2}}{h\sqrt{\pi}} \vec{\sigma} \times (\vec{v}_+(\vec{r}_0) - \vec{v}_-(\vec{r}_0)) \exp\left(-\frac{\zeta^2}{2h^2}\right); \quad (7)$$

$$h = \sqrt{\frac{v}{-\vec{\sigma}_0 \cdot \hat{S}(\vec{r}_0) \cdot \vec{\sigma}_0}}; \quad (8)$$

$$\hat{S}_{\alpha\beta}(\vec{r}_0) = \frac{1}{2}\partial_{\alpha}\partial_{\beta}\Phi_+(\vec{r}_0) + \frac{1}{2}\partial_{\alpha}\partial_{\beta}\Phi_-(\vec{r}_0) \quad (9)$$

With the inequality $S_{nn} < 0$ satisfied, this width h will be real positive.

It is important to understand that this inequality breaks the reversibility of the Euler equation: the strain is an odd variable for time reflection, although it is even for space reflection.

This inequality is a dynamic mechanism of the irreversibility of the turbulent flow: the vorticity can collapse only to the surface with negative normal strain.

2. The exact analytic solution of the CVS equations

In the first part of this study¹⁰ we have found some equations (CVS equations) for the velocity field and this surface in cylindrical geometry.

The motivation for cylindrical geometry is two-fold. First, this is the only known case of exactly solvable stability equations. Second, several DNS indicates that the dominant vortex structures are long tubes corresponding to the cylindrical geometry. There are also theoretical arguments we present below, justifying such solutions as self-consistent ones.

Let us describe, generalize and solve the cylindrical CVS equations before studying the associated turbulent statistics. As we shall see, there is a simple analytic solution to this generalized equation, unlike the original one.¹⁰

2.1. Stationary Vortex Sheets and Double Layer Potentials

The steady closed vortex surface \mathcal{S} can be treated within the framework of hydrostatics, as it was recently advocated in our paper.¹¹

In the 3D space inside and outside the surface $\mathcal{S}^{\pm} : \partial\mathcal{S}^{\pm} = \mathcal{S}$ there is no vorticity so that the flow can be described by a potential $\Phi(\vec{r})$ with the gap $\Gamma = \Delta\Phi$ on the surface.

The solution suggested in our previous paper¹⁰ is a well-known double-layer potential from electrostatics.¹⁴ The outside potential is given by the Coulomb

integral with dipole density Γ plus a background constant strain potential

$$\Phi_+(\vec{r}) = \frac{1}{2} W_{\alpha\beta} r_\alpha r_\beta - \frac{1}{4\pi} \int_S \Gamma(\vec{r}') d^2\sigma_\alpha(\vec{r}') \partial_\alpha \frac{1}{|\vec{r} - \vec{r}'|}; \quad (10)$$

$$d^2\sigma_\alpha(\vec{r}) = e_{\alpha\beta\gamma} dr_\beta \wedge dr_\gamma; \quad (11)$$

The pressure in each of the domains inside/outside is given by the Bernoulli formula

$$p_\pm = -\frac{1}{2} (\partial_\alpha \Phi_\pm(\vec{r}))^2 \quad (12)$$

The normal velocity is continuous, as one may readily check. Schematically, this check goes as follows. This formula involves the normal derivative of the Coulomb kernel. Using the Laplace equation on each side of the surface, we reduce the second normal derivative to the minus tangent Laplacian of the Coulomb kernel, which is the same on both sides.

The tangent velocity, on the other hand, has a gap $\Delta\vec{v}$. This gap arises because of the gap in the potential

$$\Gamma = \Phi_+(\vec{r}) - \Phi_-(\vec{r}); \quad \forall \vec{r} \in \mathcal{S}; \quad (13)$$

$$\Delta\vec{v} = \vec{\nabla}\Gamma \quad (14)$$

Both potentials are solutions to the corresponding Neumann problem outside and inside the surface with a fixed shape.

Therefore, the boundary values of the strain are some nonlocal functionals of the surface shape. The CVS equations lead to the nonlinear functional equation for the surface shape, which looks hopeless in the general case.

However, these equations can be solved analytically with cylindrical geometry, thanks to the magic of complex analysis.

2.2. CVS Equation for Cylindrical Geometry

In the previous paper,¹⁰ we considered a cylindrical geometry, where the piecewise harmonic potential has the following form:

$$\Phi_\pm(x, y, z) = \frac{1}{2} ax^2 + \frac{1}{2} by^2 + \frac{1}{2} cz^2 + \text{Re } \phi_\pm(\eta); \quad (15)$$

$$a + b + c = 0, \quad a \leq b \leq c; \quad c > 0, \quad a < 0; \quad (16)$$

$$\eta = x + iy; \quad (17)$$

$$\phi_\pm(\eta) = \frac{1}{2\pi i} \int d\Gamma_\pm(\theta) \log(\eta - C(\theta)); \quad (18)$$

$$v_z = cz; \quad (19)$$

$$V_\pm(x, y) = v_x - iv_y = ax - iby + F_\pm(x + iy); \quad (20)$$

$$F_\pm(\eta) = \phi'_\pm(\eta); \quad (21)$$

Here $C(\theta)$ is a complex periodic function of the angle $\theta \in (0, 2\pi)$ parametrizing the closed loop C . We simplified the notations compared to,¹⁰ now we denote the ordered eigenvalues of the background strain tensor as a, b, c .

The geometry is as follows. The vortex surface corresponds to the parallel transport of the xy loop C in in the third dimension z . Thus, at some point on the surface, the local tangent frame is

$$\vec{E}_1 = \left(\frac{\mathbf{Re} C'}{|C'|}, \frac{\mathbf{Im} C'}{|C'|}, 0 \right); \quad (22)$$

$$\vec{E}_2 = (0, 0, 1); \quad (23)$$

$$\vec{E}_3 = \left(\frac{\mathbf{Im} C'}{|C'|}, -\frac{\mathbf{Re} C'}{|C'|}, 0 \right) \quad (24)$$

The first two orthogonal vectors define the tangent plane, and the third one $\vec{E}_3 = \vec{E}_1 \times \vec{E}_2$ corresponds to the normal $\vec{\sigma}$ to the surface. Do not confuse the z direction with the normal – this is one of the two tangent directions. (See Fig.1).

The functions $\Gamma_{\pm}(\theta)$ in this solution can be complex in general; the circulation will depend on the real part.

The double-layer potential studied in the previous paper,¹⁰ corresponds to the real $\Gamma_+(\theta) = \Gamma_-(\theta)$. In that particular case, the reparametrization of the curve would eliminate this function so that the solution would be parametrized by the loop $C(\theta)$ modulo diffeomorphisms.

As we see it now, the condition of real and equal $\Gamma_{\pm}(\theta)$ is unnecessary. We shall find simple analytic solutions by dropping this restriction.

The CVS equations were reduced in¹⁰ to the complex equation (with V_{\pm} denoting the boundary values at each side of the surface)

$$V_+(C(\theta)) + V_-(C(\theta)) = 0; \quad (25)$$

The condition of vanishing normal velocity at each side of the steady surface can be reduced to the following real equation

$$\mathbf{Im} C'(\theta) V_-(C(\theta)) = 0; \quad (26)$$

The normal velocity on another side will also vanish in virtue of (25).

These two equations were derived in¹⁰ under assumptions of real $d\Gamma_{\pm}(\theta)$ in (19) which we find unnecessary and drop now.

In Appendix A., we re-derive these two equations without extra assumptions.

It follows from equation (25) that one of the two eigenvalues of the local tangent strain at the surface vanishes. This vanishing eigenvalue corresponds to the velocity gap $\Delta V = V_+ - V_- = -2V_-$ as an eigenvector.

The way to prove this is to note that differentiation of (25) by θ reduces to projecting the complex derivatives of $V_+(C) + V_-(C)$ on the complex tangent vector $C'(\theta)$. As the θ derivative of $V_+(C) + V_-(C)$ is zero in virtue of (25), so is the projection of the strain in the direction of the curve tangent vector $C'(\theta)$.

There is no normal velocity gap (as both normal velocities are zero), nor is there any gap in the z component of velocity $v_z = cz$. Thus, the velocity gap aligns with the curve tangent vector $C'(\theta)$, and therefore the strain along the velocity gap vanishes. Direct calculation in Appendix A supports this argument.

The other eigenvalue S_{nn} , corresponding to the eigenvector $\vec{\sigma} = \vec{E}_3$ normal to the surface, is then uniquely fixed by the condition of vanishing trace of the local strain tensor.

The third eigenvalue c corresponds to the eigenvector \vec{E}_2 of our cylindrical tube.

Therefore, the normal component of the strain tensor is

$$S_{nn} = -c \quad (27)$$

2.3. Spontaneous breaking of time-reversal symmetry

As the largest c of the three ordered numbers a, b, c with the sum equal to 0 is always positive (unless all three are zero), we have a negative normal strain as required by the stability of the Navier-Stokes equation in the local tangent plane.

This condition does not restrict the background strain tensor, contrary to some of our previous statements. The irreversibility of turbulence manifests itself in the negative sign of the normal strain on the surface, which is true for arbitrary nonzero eigenvalues a, b, c .

The stability conditions rather restrict the vortex tube shape: its axis aligns with the leading eigenvector of the background strain, and its profile loop adjusts to the local strain to annihilate its tangent projection.

The cylindrical shape of the vortex tube, unlike the general shape, guarantees the negative sign of the normal strain. Perhaps we are dealing with the spontaneous emergence of cylindrical symmetry at the expense of breaking the time-reversal symmetry from the stability condition.

The maximal value of the normal strain on the closed vortex surface represents a functional of its shape. So, the problem is to find under which conditions this maximal value is negative. The potential being harmonic, this normal strain equals minus the surface Laplacian of the boundary value of potential.

Thus, we are dealing with the minimal value of the surface Laplacian of a boundary value of harmonic potential on a closed surface, with Neumann boundary conditions at this surface. Under which conditions is this minimal value positive? If the answer is: only for the cylindrical surface, then the stability requires a cylindrical symmetry.

This important problem deserves further study.

The Euler equation is invariant under time reversal, changing the sign of the strain. Without the CVS boundary conditions, both signs of the normal strain would satisfy the stationary Euler equation. Therefore, this CVS vortex sheet represents a dynamical breaking of the time-reversal symmetry.

Out of the two time-reflected solutions of the Euler equation, only the one with

the negative normal strain survives. If virtually created as a metastable phase, the other one dissolves in the turbulent flow, but this remains stable.

Technically this instability displays itself in the lack of the real solutions of the steady Navier-Stokes equation for positive S_{nn} . The Gaussian profile of vorticity as a function of normal coordinate formally becomes complex at positive S_{nn} , which means instability or decay in the time-dependent equation. In¹² the authors verified this decay/instability process. The time-dependent Navier-Stokes equation was solved numerically in the vicinity of the steady solution with arbitrary background strain. Only the Burgers-Townsend solution corresponding to our CVS conditions on the strain was stable.

The breaking of time-reversal symmetry of the Euler dynamics is not driven by some external forces but rather is spontaneously created by internal Navier-Stokes dynamics. The result of this microscopic stability mechanism of the Navier-Stokes dynamics is the CVS boundary conditions added to the ambiguous Euler dynamics of the vortex sheets.

2.4. Complex Curves

Let us now proceed with the exact solution of the CVS equations.

The CVS equations for the cylindrical geometry reduce to the equation (26) for the boundary loop $C(\theta)$ plus a complex equation $V_+(x, y) + V_-(x, y) = 0$ at the loop $(x, y) \in C$.

Consider two complex functions involved in this equation: $F_-(\eta)$ inside the loop, $F_+(\eta)$ outside. These two functions are related through the boundary condition

$$F_+(\eta) + F_-(\eta) + (a - b)\eta - c\bar{\eta} = 0; \forall \eta \in C; \quad (28)$$

Let us look for the linear solution of the Laplace equation inside (constant strain):

$$F_-(\eta) = (p + \imath q)\eta \quad (29)$$

with some real p, q .

The vanishing normal velocity from the inside leads to the differential equation for $C(\theta)$.

$$\mathbf{Im} \left((2p + a - b + 2\imath q)C(\theta) - c\bar{C}(\theta) \right) C'(\theta) = 0 \quad (30)$$

This equation is integrable for arbitrary parameters. We shall use two dimensionless parameters γ, β to parametrize p, q as follows:

$$p + \imath q = \frac{b - a}{2} + \frac{ce^{-2\imath\beta}}{2(2\gamma + 1)}; \quad (31)$$

The general solution of (30) in polar coordinates reads¹⁵ (up to an arbitrary normalization constant)

$$C(\theta) = e^{i\beta}(1 + i\tau)\tau^\gamma; \quad (32)$$

$$\tau = \tan \theta \quad (33)$$

This solution applies when τ^γ is real. We analyse various unbounded solutions of this equation in Appendix B.

The next section analyzes finite periodic solutions relevant to the turbulent statistics we develop in this paper.

2.5. Finite Periodic Solutions

The periodic solution is given by an analytic continuation of the basic solution to the negative τ

$$C(\tau) = e^{i\beta}\tau^\gamma(1 + i\tau); \quad (34)$$

$$-\tau_m < \tau < \tau_m; \quad (35)$$

$$\tau_m = \tan \frac{\pi\gamma}{2}; \quad (36)$$

$$C(-\tau) = e^{i(2\beta+\pi\gamma)}\bar{C}(\tau) \text{ for } \tau > 0; \quad (37)$$

$$C(0) = C(i) = 0; \quad (38)$$

$$C(\tau_m) = C(-\tau_m) = e^{i(\beta+\pi\gamma/2)}\tau_m^\gamma\sqrt{1 + \tau_m^2} \quad (39)$$

These finite closed curves exist in the intervals where $\gamma > 0, \tan(\pi\gamma/2) > 0$, i.e.

$$0 < \gamma \pmod{2} < 1 \quad (40)$$

The area inside this curve (Fig.2)

$$Area(C) = \frac{1}{2}\mathbf{Im} \int_{-\tau_m}^{\tau_m} d\tau \bar{C}(\tau)C'(\tau) = \frac{\tau_m^{2\gamma+1}}{2\gamma+1}; \quad (41)$$

and the perimeter (Fig. 3):

$$|C| = \int_{-\tau_m}^{\tau_m} d\tau |C'(\tau)| = G(\gamma); \quad (42)$$

$$G(\gamma) = \frac{\gamma^2}{\gamma+1} \log \frac{(\gamma+1)\tau_m + B(\gamma)}{\gamma} + \tau_m B(\gamma); \quad (43)$$

$$B(\gamma) = \sqrt{\gamma^2 + (\gamma+1)^2\tau_m^2} \quad (44)$$

The linear function $F_-(\eta) = (p + iq)\eta$ has to satisfy the equation (30) for both signs of τ with negative τ branch corresponding to the complex conjugate value $(p - iq)\bar{\eta}$. The true reason for this requirement of complex conjugation will be explained below.

This provides complex equation

$$(p + iq)e^{i\pi\gamma} = (p + iq)|_{\beta \Rightarrow \beta + \pi\gamma} \quad (45)$$

Substituting (31) we get complex equation for two parameters β, γ

$$\left(\frac{b-a}{2} + \frac{ce^{-2i\beta}}{2(2\gamma+1)} \right) e^{i\pi\gamma} = \frac{b-a}{2} + \frac{ce^{-2i\beta-2\pi i\gamma}}{2(2\gamma+1)} \quad (46)$$

This equation is analyzed in.¹⁶ There are two solutions for β

$$\beta_k = \frac{\pi k}{2} - \frac{\pi\gamma}{2}; k = 0, 1 \quad (47)$$

Note that these two solutions correspond to symmetry relation

$$C(-\tau) = \pm \bar{C}(\tau) \text{ for } \mathbf{Im} \tau = 0; \quad (48)$$

This symmetry is a real motivation for the requirement of complex conjugation of $p \pm iq$ on two sides of the branch cut.

These solutions lead to the two parametric solutions of a as a function of γ

$$a_0 = c \frac{\cos(\pi\gamma) - \gamma}{2\gamma + 1}; \quad (49)$$

$$a_1 = -c \frac{\gamma + \cos(\pi\gamma) + 1}{2\gamma + 1}; \quad (50)$$

The second solution a_1 covers the physical region $-2c < a < -\frac{1}{2}c$ when γ varies in lower parts of the stability zones (40). However, at some critical values of γ

$$\gamma_c = \frac{2}{3} \pmod{2} \quad (51)$$

the branch a_1 crosses the upper boundary $a = -\frac{1}{2}c$ and goes above the physical region. At this point there is a phase transition to the branch a_0 with $\beta = \beta_0$, which enters the physical region at the same point $\gamma = \gamma_c, a = -c/2$. (Fig. 4)

Thus, the stable distribution of the ratio $\frac{a}{c}$ between -2 and $-\frac{1}{2}$ corresponds to the phase β_1, a_1 . The value of γ is given by the solution of transcendental equation

$$(2a + c)\gamma + c + a + c \cos(\pi\gamma) = 0 \quad (52)$$

and it varies between $0, \frac{2}{3}$ modulo 2.

Note that the area and perimeter of the loop $C(\tau)$ stays finite in this solution in the whole range of a/c . Maximal length is

$$\max|\eta| = 2\sqrt[3]{3} \quad (53)$$

At Fig.5 we show the plot of the maximal loop together with the loop height as a function of γ . The resulting formula for $p + iq$ reads

$$p + iq = e^{-i\frac{\pi\gamma}{2}} \frac{\cos \frac{\pi\gamma}{2}}{(2\gamma + 1)} \quad (54)$$

2.6. The velocity field and circulation

Let us now study the complex velocity of the flow.

First, we need to reconstruct the inner function from its boundary values. To do this, let us introduce new complex variable $w = -\tau^2$ and parametric representation

$$P(w) = \iota w^{\frac{\gamma}{2}}(1 - \sqrt{w}); \quad (55)$$

$$F_-(P(w)) = f(w); \quad (56)$$

$$f(-\tau^2 + \iota 0) = \frac{\cos \frac{\pi\gamma}{2}}{(2\gamma + 1)} \tau^\gamma (\iota + \tau); \quad (57)$$

$$f(-\tau^2 - \iota 0) = \frac{\cos \frac{\pi\gamma}{2}}{(2\gamma + 1)} \tau^\gamma (\iota - \tau); \quad (58)$$

The loop $C(\tau)$ is mapped to the contour encircling the interval from $-\tau_m^2$ to 0 in the complex w plane. The upper/lower side of this interval corresponds to the right/left side of the vertical loop at Fig.5.

The Riemann surface of the function $P(w)$ for $\gamma = 1/3$ is shown at Fig.6.

The function $f(w)$ takes minus complex-conjugate values at two sides of the cut from $-\tau_m^2$ to 0. This allows us to reconstruct it by a Cauchy integral

$$f(w) = \int_0^{\tau_m^2} \frac{dz \mathbf{Re} f(-z + \iota 0)}{\pi \iota (w + z)} = \frac{\cos \frac{\pi\gamma}{2}}{(2\gamma + 1)} \int_0^{\tau_m^2} \frac{dz z^{\frac{1}{2}(\gamma+1)}}{\pi \iota (w + z)} \quad (59)$$

This integral reduces to the hypergeometric function

$$f(w) = - \frac{2i \cos \left(\frac{\pi\gamma}{2} \right) \tau_m^{\gamma+3} {}_2F_1 \left(1, \frac{\gamma+3}{2}; \frac{\gamma+5}{2}; -\frac{\tau_m^2}{w} \right)}{\pi(\gamma + 3)(2\gamma + 1)w} \quad (60)$$

This function is holomorphic outside the cut in complex w plane. Its complex map is shown at Fig. 7.

The outside function also takes minus complex-conjugate values at two sides of the cut:

$$F_+(P(w)) = g(w); \quad (61)$$

$$g(w) = -f(w) - (c + 2a)P(w) + c\bar{P}(w) \text{ for } w \in (-\tau_m^2, 0); \quad (62)$$

Therefore, it is given by a similar Cauchy integral

$$g(w) = \iota \int_0^{\tau_m^2} \frac{dz \mathbf{Re} (f(-z + \iota 0) + 2(c + a)P(-z + \iota 0))}{\pi(w + z)} \quad (63)$$

The computation¹⁶ yields:

$$g(w) = \frac{2ic \sin\left(\frac{\pi\gamma}{2}\right) \tan^{\gamma+2}\left(\frac{\pi\gamma}{2}\right)}{\pi(2\gamma+1)} (A(w) - B(w)); \quad (64)$$

$$A(w) = \frac{(2\gamma + \cos(\pi\gamma) + 2) {}_2F_1\left(1, \frac{\gamma+3}{2}; \frac{\gamma+5}{2}; -\frac{\tan^2\left(\frac{\pi\gamma}{2}\right)}{w}\right)}{(\gamma+3)w}; \quad (65)$$

$$B(w) = \frac{(2\gamma + \cos(\pi\gamma) + 1) {}_2F_1\left(1, \frac{\gamma+2}{2}; \frac{\gamma+4}{2}; -\frac{\tan^2\left(\frac{\pi\gamma}{2}\right)}{w}\right)}{(\gamma+2)w} \quad (66)$$

The complex map of $g(w)$ is shown on Fig. 8. There are no singularities of $g(w)$ outside the loop.

There is a square root singularity in the inverse function $w(\eta)$ solving implicit equation

$$P(w) = \eta \quad (67)$$

The positions w_n, η_n of this singularity are located at the vanishing derivative $P'(w_n) = 0$

$$w_n = e^{2\pi i n} \frac{\gamma^2}{(\gamma+1)^2}; \quad (68)$$

$$\eta_n = i w_n^{\frac{\gamma}{2}} (1 - \sqrt{w_n}) \quad (69)$$

Here n is the number of the sheet of the Riemann surface. For $n = 0$ the position of this singularity is at imaginary η_0 inside the loop; for the next sheet $n = 1$ the position η_1 is outside the loop.

Thus, the outside function $F_+(\eta)$ corresponds to w varying on the $n = 0$ sheet, and the inside function $F_-(\eta)$ corresponds to the $n = 1$ sheet of this Riemann surface.

Technically, this means that $F_{\pm}(\eta)$ are parametrized as:

$$F_+(P(w)) = g(w); \quad (70)$$

$$F_-\left(P\left(we^{2i\pi}\right)\right) = f(w) \quad (71)$$

At the loop, where these two sheets meet, there is a finite gap $\Delta F(\tau) = g(-\tau^2) - f(-\tau^2)$ between branches.

The potential gap Γ is expressed in terms of this ΔF :

$$\Gamma(\tau) = \int_{-\tau_m}^{\tau} d\vec{r}(\tau) \cdot \Delta\vec{v} = \mathbf{Re} \int_{-\tau_m}^{\tau} d\tau P'(\tau) \Delta F(\tau); \quad (72)$$

The integral computes to the following

$$\Gamma(\tau) = \frac{c}{4(2\gamma + 1)^2} (\tau^{2\gamma} H(\tau) - \tau_m^{2\gamma} H(\tau_m)); \quad (73)$$

$$H(t) = - \left((2\gamma + 1) \left((4\gamma + 5)\tau^2 + (\tau^2 + 1) \cos(2\pi\gamma) - 4\gamma - 1 \right) \right) - 4\gamma\tau \sin(\pi\gamma) - 2\tau \cos(\pi\gamma)(2\gamma\tau - 2\sin(\pi\gamma) + \tau) \quad (74)$$

The circulation of velocity gap around the tube vanishes

$$\Delta\Gamma = \Gamma(\tau_m) = 0; \quad (75)$$

As we discuss below, with zero circulation, the divergent term in the energy density vanishes.

2.7. wedges and Falkner-Skan boundary layer

The curve is not smooth (there is a $\delta_0 = \pi\gamma \bmod 2\pi$ inner angle at origin and

$$\delta_1 = \pi(1 - \gamma) - 2 \arg \left(\gamma + i\gamma \cot \left(\frac{\pi\gamma}{2} \right) + 1 \right) \bmod 2\pi \quad (76)$$

inner angle at $\tau = \tau_m$.

The smooth curve would have $\delta_0 = \delta_1 = \pi$.

The wedges arising at these two points require the special solution of the Navier-Stokes equation in their vicinity to verify their stability.

Fortunately, this special solution was discovered by Falkner and Skan 90 years ago.^{17,18} It was supposed to describe the viscid incompressible flow past the wedge, but it applies without changes to the two wedges of our tube, as the boundary condition of vanishing normal velocity is the same.

The outer region corresponds to the Falkner-Skan solutions with $\beta_{FS} = \gamma \bmod 2, \frac{\delta_1}{\pi}$. The inner region corresponds to complementary angles, or $\beta'_{FS} = 2 - \beta_{FS}$.

The Falkner-Skan solution is stable (see reference in¹⁸) for

$$-0.198838 \leq \beta_{FS} \leq 4/3 \quad (77)$$

Both inequalities are satisfied in every stability zone (40). For the corner at $\tau = 0, \beta_{FS} = (\gamma, 2 - \gamma) \bmod 2$ it is obvious, and for the second corner, at $\tau = \tau_m$ it follows from the plot at Fig. 9.

2.8. Minimizing Euler Energy

Let us now compute the energy of the vortex surface as a Hamiltonian system.^{19,20} There is a regular part related to the background strain. This part is not involved in the minimization we are interested in; it depends on a, b, c , which are external parameters for our problem.

The internal part of the Hamiltonian is directly related to the potential gap Γ we have computed in the previous section.

$$H_{int} = \int_{\vec{r}_1, \vec{r}_2 \in \mathcal{S}} d\Gamma(\vec{r}_1) \wedge d\vec{r}_1 \cdot d\Gamma(\vec{r}_1) \wedge d\vec{r}_1 \frac{1}{8\pi|\vec{r}_1 - \vec{r}_2|} \quad (78)$$

In our case of cylindrical surface

$$d\Gamma(\vec{r}_1) \wedge d\vec{r}_1 = d\Gamma(\tau) \{0, 0, dz\} \quad (79)$$

and we have a separation of variables τ, z .

The integration over z_1, z_2 provides the total length $L \rightarrow \infty$ of the cylinder times logarithmically divergent integral over $z_1 - z_2$. We limit this integral to the interval $(-L, L)$ and compute it exactly

$$\int_{-L}^L \frac{1}{8\pi\sqrt{\eta^2 + z^2}} dz = \frac{\log\left(\frac{2L(\sqrt{\eta^2 + L^2} + L)}{\eta^2} + 1\right)}{8\pi} \quad (80)$$

Then we expand it for large L

$$\int_{-L}^L \frac{1}{8\pi\sqrt{\eta^2 + z^2}} dz \rightarrow \frac{\log(2L) - \log|\eta|}{4\pi} + O\left(\frac{\eta^2}{L^2}\right) \quad (81)$$

Thus we get in our case

$$\frac{H_{int}}{L} = \log(2L) \frac{(\Delta\Gamma)^2}{4\pi} - \frac{1}{8\pi} \int d\Gamma(\tau_1) d\Gamma(\tau_2) \log|C(\tau_1) - C(\tau_2)|; \quad (82)$$

At $L \rightarrow \infty$ the first term is the leading one. Minimization of the energy leads to the condition

$$\Delta\Gamma = 0 \quad (83)$$

Therefore, our solutions with zero circulation are singled out by the requirement of minimization of energy.

Once the divergent term vanishes, one can compute the rest of the energy.

We do not see a point in this computation compared to observable quantities such as the energy dissipation and the Wilson loop.

3. Turbulent Statistics

What is the physical origin of the constant background strain $W_{\alpha\beta}$ which we used in our solution?

Traditionally, the ad hoc Gaussian random forces are added to the Navier-Stokes equation to simulate the effects of the unknown inner randomness.

We do not think that this beautiful equation needs any crutches; it can walk all by itself.

In our theory, the random forces come from many remote vortex structures, contributing to the background velocity field via the Biot-Savart law.

These forces are not arbitrary; they are rather self-consistent, like a mean-field in ordinary statistical mechanics.

3.1. *The induced random background strain*

Let us assume that the space is occupied by some localized CVS structures far from each other. In other words, let us consider an ideal gas of vortex tubes.

This ideal gas approximation is close to reality, where the vorticity occupies a small subset of the physical space. The singular vortex structures are forming long tubes in DNS.^{1,2}

We shall see below that the mean size R_0 of the surface is small compared to the mean distance \bar{R} between them in the turbulent limit $\nu \rightarrow 0, \mathcal{E} = \text{const}$. This vanishing size vindicates the assumptions of the low-density ideal gas.

In such an ideal gas, we can neglect the collision of these extended particles, but not the long-range effect of the strain they impose on each other.

The Biot-Savart formula for the velocity field induced by the set of remote localized vorticity tubes B

$$\vec{v}(\vec{r}) = \sum_B \int_B d^3r' \frac{\vec{\omega}(\vec{r}') \times (\vec{r}' - \vec{r})}{4\pi|\vec{r} - \vec{r}'|^3} \quad (84)$$

falls off as $1/r^2$ for each tube, like an electric field from the charged body.

Note that all vortex structures in the volume contribute to this background velocity field, adding up to a large number of small terms at every point in space.

If there are many such tubes distributed in space with small but finite density, we would have the "night sky paradox." The tubes spread on the far away sphere will compensate the inverse distance squared for a divergent distribution like $\int R^2 dR/R^2$.

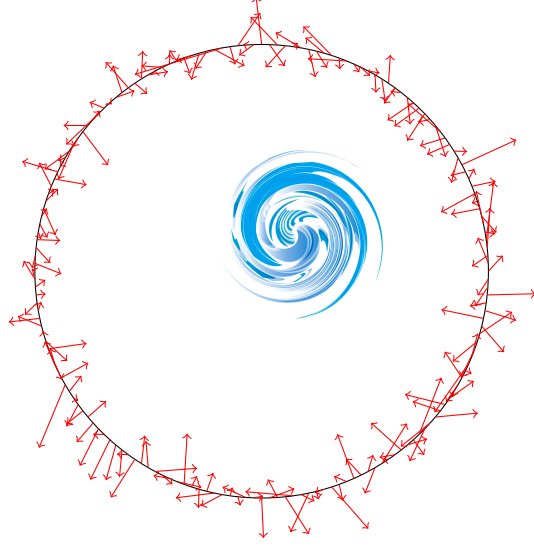
This estimate is, of course, wrong, as the velocity contributions from various tubes are uncorrelated, so there is no coherent mean velocity.

Moreover, a Galilean transformation would remove the finite background velocity, so it does not have any physical effects.

However, with the strain, there is another story. Strain coming from remote vortex tubes

$$W_{\alpha\beta}(\vec{r}) = e_{\alpha\mu\gamma} \partial_\beta \partial_\gamma \sum_B \int_B d^3r' \frac{\omega_\mu(\vec{r}')}{4\pi|\vec{r} - \vec{r}'|} \quad (85)$$

falls off as $1/r^3$, and this time, there could be a mean value \bar{W} , coming from a large number of random terms from various tubes with distribution $R^2 dR/R^3 \sim dR/R$.



This picture symbolizes the vortex tube under consideration (blue vortex symbol) surrounded by other remote tubes on a large sphere (orange arrows). The arrows symbolize the directions of these remote tubes, which follow the local strain main axis and point in random directions.

The space symmetry arguments and some refined arguments we present in the next section tell us that averaging over the directions of the tube centers $\vec{R} = \vec{r}' - \vec{r}$ completely cancels this mean value.

The Central Limit Theorem suggests (within our ideal vortex gas model) that such a strain would be a Gaussian tensor variable, satisfying the normal distribution of a symmetric traceless matrix with zero mean (see Appendix C.)

$$dP_{\sigma}(W) \propto \prod_i dW_{ii} \prod_{i < j} dW_{ij} \delta\left(\sum_i W_{ii}\right) \exp\left(-\frac{\text{tr} W^2}{2\sigma^2}\right) \quad (86)$$

The parameter σ is related to the mean mean square of the random matrix. In n dimensional space

$$\frac{(n+2)(n-1)}{2} \sigma^2 = \langle \text{tr} W^2 \rangle \quad (87)$$

The Gaussian random matrices were studied extensively in physics and mathematics. For example, in²¹ the distribution of Gaussian random symmetric matrix (Gaussian Orthogonal Ensemble, $GOE(n)$) is presented.

We achieve the extra condition of zero trace by inserting the delta function of the matrix trace into the invariant measure. As the trace is invariant to orthogonal transformations, this projection preserves the measure's $O(n)$ invariance. We could not find any references for this straightforward extension of the $GOE(n)$ to the space of traceless symmetric matrices.

Separating $SO(3)$ rotations $\Omega \in S_2$, we have the measure for eigenvalues a, b, c :

$$dP_\sigma(W) = \frac{1}{4\pi} d\Omega da db dc \delta(a+b+c) P_\sigma(a, b, c); \quad (88)$$

$$P_\sigma(a, b, c) = \sqrt{\frac{3}{\pi}} \theta(b-a) \theta(c-b) (b-a)(c-a)(c-b) \exp\left(-\frac{a^2+b^2+c^2}{2\sigma^2}\right); \quad (89)$$

$$5\sigma^2 = \langle a^2 + b^2 + c^2 \rangle \quad (90)$$

3.2. Energy dissipation and the perimeter distribution

The general formula¹⁰ for the surface dissipation reads

$$\mathcal{E} = \frac{\sqrt{\nu}}{2\sqrt{\pi}} \int dS \sqrt{-S_{mn}} (\Delta \vec{v})^2; \quad (91)$$

As we noticed in the previous work¹⁰ this surface dissipation is conserved on CVS surfaces.

Without CVS as a stability condition, the dissipation itself would not be an integral of motion, undermining the hypothesis of the steady energy flow, which is central to any modern theory or model of turbulence.

For our closed loop solution the energy dissipation integral¹⁶ reduces to the following expression (where we restore the implied spatial scale R_0 in the curve $C(\tau)$)

$$\frac{\mathcal{E}}{L\sqrt{\nu}} = c^{\frac{5}{2}} R_0^3 \Phi(\gamma); \quad (92)$$

$$\Phi(\gamma) = \frac{\tau_m^{3\gamma} (A(\gamma) + B(\gamma))}{3(2\gamma + 1)^2}; \quad (93)$$

$$A(\gamma) = \frac{3\gamma\tau_m^2(4\gamma(2\gamma+5) + 4(2\gamma+3)\cos(\pi\gamma) + (4\gamma+5)\cos(2\pi\gamma) + 15)}{3\gamma+2}$$

$${}_2F_1\left(-\frac{1}{2}, \frac{3\gamma}{2} + 1; \frac{3\gamma}{2} + 2; -\frac{(\gamma+1)^2\tau_m^2}{\gamma^2}\right); \quad (94)$$

$$B(\gamma) = \left(8\gamma^2 + 4\gamma - (4\gamma+1)\cos(2\pi\gamma) + 1\right)$$

$${}_2F_1\left(-\frac{1}{2}, \frac{3\gamma}{2}; \frac{3\gamma}{2} + 1; -\frac{(\gamma+1)^2\tau_m^2}{\gamma^2}\right); \quad (95)$$

$$\tau_m = \tan\left(\frac{\pi\gamma}{2}\right); \quad (96)$$

Here ${}_2F_1(a, b; c; z)$ is a hypergeometric function.

The plot of $\Phi(\gamma)$ in the physical region $0 < \gamma < \frac{2}{3}$ is shown at Fig 10. At the end of the physical region it takes a finite value

$$\Phi\left(\frac{2}{3}\right) = \frac{2\left(632711\sqrt{79} - 11722\right)}{459375} = 24.4329 \quad (97)$$

The normalized distribution of the index γ which follows from the random matrix distribution with our parametrization $a = a_1$ reads¹⁶

$$dW(\gamma) = d\gamma \frac{3\sqrt{3}(3\gamma + 1 - \cos(\pi\gamma))(3\gamma + \cos(\pi\gamma) + 2)(2\cos(\pi\gamma) + 1)}{8(3\gamma(\gamma + 1) + \cos^2(\pi\gamma) + \cos(\pi\gamma) + 1)^{5/2}} \\ (\pi(2\gamma + 1)\sin(\pi\gamma) + 2\cos(\pi\gamma) + 1) \quad (98)$$

We plot this distribution at Fig. 10.

The variable $r = \frac{\varepsilon}{\sigma}$ is distributed as

$$dW(r) = \frac{8}{3\sqrt{\pi}} r^4 e^{-r^2} dr; \quad (99)$$

The scale parameter R_0 can be expressed in terms of perimeter $|C|$ of the loop

$$R_0 = \frac{|C|}{G(\gamma)} \quad (100)$$

We can now relate this random variable with loop perimeter $|C|$ of the tube

$$r = \left(\frac{R\varepsilon}{|C|}\right)^{\frac{6}{5}} H(\gamma); \quad (101)$$

$$H(\gamma) = \frac{G(\gamma)^{\frac{6}{5}}}{\Phi(\gamma)^{\frac{2}{5}}}; \quad (102)$$

$$R\varepsilon = \left(\frac{L\sqrt{v\sigma^5}}{\varepsilon}\right)^{\frac{1}{3}}; \quad (103)$$

$$\frac{dr}{r} = \frac{6}{5} \frac{d|C|}{|C|} \quad (104)$$

Thus, we get the distribution of perimeter

$$\frac{dW(r)}{d|C|} = \frac{48}{15\sqrt{\pi}} \frac{1}{|C|} \int_0^{\frac{2}{3}} d\gamma e^{-r^2(\gamma, |C|)} r^5(\gamma, |C|); \quad (105)$$

$$r(\gamma, |C|) = \left(\frac{R\varepsilon}{|C|}\right)^{\frac{6}{5}} H(\gamma)^{\frac{2}{5}} \quad (106)$$

We show at Fig.12 the log-log plot of this distribution.

This log-log distribution is a completely universal function, up to shifts in the x-axis.

In principle, existing DNS databases such as³ allows one to extract the distribution of the tube radius and verify our solution. This work would take a statistical

analysis of terabytes of vorticity data in a fully developed isotropic turbulent flow. Such a large computational project merits a separate publication.

3.3. Dilute gas of vortex tubes in mean-field approximation

Let us elaborate on the idea of a dilute gas of vortex tubes and compute the strain variance.

Consider a large number of vortex tubes, sparsely distributed in the 3D volume.

The net strain near each tube will come from the Biot-Savart formula (85), which we expand at large distances (plus symmetric terms with swapped α, β)

$$W_{\alpha\beta}(\vec{r}) = \sum_B W_{\alpha\beta}^{(B)}(\vec{r}) + \{\alpha \leftrightarrow \beta\}; \quad (107)$$

$$W_{\alpha\beta}^{(B)}(\vec{r}) \rightarrow e_{\alpha\mu\gamma} \left(\Omega_\mu \partial_\beta \partial_\gamma + \Omega_{\mu\lambda} \partial_\beta \partial_\gamma \partial_\lambda + \dots \right) \frac{1}{4\pi|\vec{r} - \vec{r}_B|}; \quad (108)$$

$$\Omega_\mu = \int_B d^3 r' \omega_\mu(\vec{r}'); \quad (109)$$

$$\Omega_{\mu\lambda} = \int_B d^3 r' \omega_\mu(\vec{r}') r'_\lambda \quad (110)$$

Note that while the Navier-Stokes equation is nonlinear, this linear relation between the local strain and contributions from each vortex tube is **exact**, as it follows from the linear Poisson equation relating velocity to vorticity.

Therefore, the interaction between tubes decreases with distance by the power law, which justifies the ideal gas picture in the case of sparsely distributed vortex tubes. There is no such thing as "nonlinear interaction between vortex structures" over large distance $\vec{r} - \vec{r}_B$ in the Navier-Stokes equation.

Another comment is in order. With cylindrical geometry, the tubes are infinite, and the integrals for multipole moments $\Omega_{\mu\dots}$ diverge.

We consider the case of large but finite tubes, assuming only the thickness of the tubes is small compared to their separation.

In the general case, one may assume that the tubes do not intersect, despite their large lengths. The well-known property says that two random infinite lines do not intersect in 3D space (though they do so in two dimensions).

In this generic case, one can use the multipole expansion for the Biot-Savart law far away from each tube B .

The contribution to the strain from each remote vortex tube will be linearly related to these multipole moments of vorticity.

These vectors and tensors are random variables with zero mean^a.

^aThe directions of these vectors in our exact solution coincide with one of the eigenvectors of the local strain tensor at the location of that particular CVS surface. Assuming random locations in space, so will the strain tensors, which is why we expect the Central Limit Theorem to apply here.

The vorticity for each vortex tube S is given by a surface integral^{19,20}

$$\omega_v(\vec{r}) = \int_S d\Gamma \wedge dr'_v \delta^3(\vec{r} - \vec{r}'); \quad (111)$$

$$\Omega_\mu = \int_S d\Gamma \wedge dr_\mu; \quad (112)$$

$$\Omega_{\mu\lambda} = \int_S d\Gamma \wedge dr_\mu r_\lambda \quad (113)$$

The first term, with net vorticity Ω_μ , vanishes in our theory with zero net circulation

$$\Omega_\mu = \delta_{\mu 3} L \oint d\Gamma(\theta) = 0 \quad (114)$$

The rotational average of the multiple derivative matrix has only one totally symmetric symmetric tensor structure

$$\begin{aligned} T_{\mu_1 \dots \mu_n} &= \left\langle \partial_{\mu_1} \dots \partial_{\mu_n} \frac{1}{|\vec{r}|} \right\rangle_{\vec{r} \in S_2} = \\ &= C \left(\delta_{\mu_1 \mu_2} \dots \delta_{\mu_{n-1} \mu_n} + \text{permutations} \right) \end{aligned} \quad (115)$$

However, the contraction over any pair of indices yields zero because $\frac{1}{|\vec{r}|}$ satisfies the Laplace equation. Therefore $C = 0$.

The number dN of the vortex structures on the large sphere would be estimated as

$$dN = 4\pi \rho(R) R^2 dR \quad (116)$$

where $\rho(R)$ is the distribution of distances between the vortex structures.

After some tensor algebra and symbolic angular integration²² we found the formula for σ with separated averaging over the unit vector on a sphere S_2 and the random tensor W

$$5\sigma^2 = \frac{9}{2\pi^2} \left\langle \Omega_{\alpha\beta}^2 \right\rangle_W 4\pi \int dR \frac{\rho(R)}{R^6}; \quad (117)$$

This distribution is normalized as

$$4\pi \int dR \rho(R) R^2 = 1 \quad (118)$$

Therefore, our expression involves a mean value of $1/R^8$

$$\left\langle \frac{1}{R^8} \right\rangle = \frac{\int dR \rho(R) R^{-6}}{\int dR \rho(R) R^2}; \quad (119)$$

$$\int dR \rho(R) R^{-6} = \frac{1}{4\pi} \left\langle \frac{1}{R^8} \right\rangle \quad (120)$$

After that, we relate the variance to the mean squared vorticity of each vortex structure and the relative distance distribution of these tubes.

$$\sigma^2 = \frac{9}{10\pi^2} \langle \Omega_{\alpha\beta}^2 \rangle_W \left\langle \frac{1}{R^8} \right\rangle \quad (121)$$

In our theory, with a cylindrical tube of size L , we find:¹⁶

$$\Omega_{\alpha\beta} = L \left(\delta_{\alpha z} I_\beta - \delta_{\beta z} I_\alpha \right); \quad (122)$$

$$I_z = 0; \quad (123)$$

$$I_x + i I_y = \oint_C d\Gamma C = cR_0^3 \frac{e^{\frac{1}{2}(-5)i\pi\gamma} \tan^{3(\gamma+1)} \left(\frac{\pi\gamma}{2} \right) S(\gamma)}{3(-1 + e^{i\pi\gamma})^3 (2\gamma + 1)(3\gamma + 1)(3\gamma + 2)}; \quad (124)$$

$$\begin{aligned} S(\gamma) = & -6\gamma - 2e^{i\pi\gamma}(3\gamma + 2) + e^{4i\pi\gamma}(6\gamma + 3) \\ & - 3e^{3i\pi\gamma}(2\gamma + 1)(12\gamma + 5) + 6e^{5i\pi\gamma}(\gamma(6\gamma + 5) + 1) + \\ & 6e^{6i\pi\gamma}(\gamma(6\gamma + 5) + 1) + 2e^{2i\pi\gamma}(3\gamma + 2)(4\gamma(6\gamma + 5) + 3) \\ & + e^{7i\pi\gamma}(6\gamma(6\gamma + 7) + 13) - 2e^{8i\pi\gamma}(2\gamma(9\gamma(4\gamma + 7) + 32) + 9) - 3 \end{aligned} \quad (125)$$

After integrating over the eigenvalues a, b, c , using formulas for R_0 and $a_a(\gamma)$ from the previous section, we find¹⁶ the following expression for the variance of strain

$$\sigma^2 = 4.04723\sigma^2 (R_\mathcal{E})^{\frac{12}{5}} L^2 |C|^{\frac{18}{5}} \left\langle \frac{1}{R^8} \right\rangle; \quad (126)$$

This brings us to the final relation between our parameters

$$\bar{R} = \left\langle \frac{1}{R^8} \right\rangle^{-\frac{1}{8}} \sim (R_\mathcal{E})^{\frac{3}{10}} L^{\frac{1}{4}} |C|^{\frac{9}{20}} \quad (127)$$

We observe that with long tubes $L \gg |C|$ the mean distance \bar{R} between them is much larger than their thickness measured by $|C|$ but smaller than their length. The probability of collision of long thin sticks in three dimensions goes to zero with a ratio of thickness to length so that the assumed conditions of the dilute gas hold.

3.4. Vortex tube fluctuations imitate multifractal

Our loop C is finite and piecewise smooth, but its shape and its perimeter $|C|$ are characterized by a random variable index γ . The fluctuating size of the vortex structure can imitate the multifractal scaling laws without any fractals present.

Let us turn our attention to the most interesting functional, the velocity difference, related to the velocity gap in our theory.

Velocity field in the CVS theory is potential everywhere in space, except the thin layers surrounding our hyperbolic vortex sheets.

The velocity difference between two neighboring points \vec{r}_1, \vec{r}_2 in the potential flow with scale as $\vec{r}_1 - \vec{r}_2$ as the harmonic potential has no singularity.

However, with some probability, these two points will be separated by a vortex surface, in which case there will be a finite gap $\Delta\vec{v}$.

The estimate of the velocity difference moments would involve integration over the translation, rotation, and eigenvalues of the strain tensor.

Schematically, assuming $\vec{r}_2 = (x_2, y_2, z)$ outside our vortex tube, and $\vec{r}_1 = (x_1, y_1, 0)$ inside, we have (with $\eta_1 = x_1 + iy_1, \eta_2 = x_2 + iy_2$):

$$\langle (\Delta\vec{v} \cdot \hat{r})^n \rangle \propto \left\langle \int_{\Sigma(\Omega)} dx_1 dy_1 dx_2 dy_2 dz (\Delta\vec{v} \cdot \hat{r})^n \right\rangle_W ; \quad (128)$$

$$\Delta\vec{v} = (\mathbf{Re} F_+(\eta_2) - \mathbf{Re} F_-(\eta_1), -\mathbf{Im} F_+(\eta_2) + \mathbf{Im} F_-(\eta_1), cz) ; \quad (129)$$

$$\Delta\vec{r} = (x_2 - x_1, y_2 - y_1, z) ; \quad (130)$$

$$\hat{r} = \frac{\Delta\vec{r}}{|\Delta\vec{r}|} ; \quad (131)$$

$$\Sigma(\Omega) : \Omega \cdot \Delta\vec{r} = (r, 0, 0) ; \quad (132)$$

The measure for the traceless random 3×3 matrices $dP_\sigma(W)$ is presented in (88). The nontrivial part is the $SO(3)$ integration measure over the 3D rotations Ω involved in that measure. The distribution of the ratio of eigenvalues a, b, c in (88) leads to the distribution of the index γ , related to the ratio a/c .

By dimensional counting, the integral in (128) has the following structure

$$\langle (\Delta\vec{v} \cdot \hat{r})^n \rangle = \int_0^\infty \frac{d|C|}{|C|} |C|^{n/3} U_n \left(\frac{|C|}{R_\varepsilon}, \frac{|C|}{r} \right) \quad (133)$$

The function $U_n(x, y)$ here will involve the PDF (105) for the perimeter $|C|$ which is almost constant at small $|C|$ but sharply decrease at large perimeters.

Other factors in the integral all grow with the perimeter of the tube as some power. Therefore, the integration over the random variable $|C|$ in the turbulent limit of distances r larger than the viscous length will reduce to some saddle point $|C|_0$ which would depend on r and n .

We do not expect this dependence to result in exact power-law $\langle (\Delta\vec{v} \cdot \hat{r})^n \rangle \propto |\Delta\vec{r}|^{\zeta(n)}$ assumed in the multifractal model. It is a more complicated function of two variables $n, \log r$. The saddle point approximation of this integral could imitate a multifractal scaling law.

Our vortex sheet solution explicitly breaks the time-reversal symmetry; therefore, the odd moments do not vanish. The interchange of the two coordinates $\vec{r}_2 \leftrightarrow \vec{r}_1$ changes the velocity field significantly.

There is a way to estimate the multifractal scaling law from our theory without computing this multidimensional integral (which we plan to do eventually).

In a recent work of Sreenivasan and Yakhot²³ it was argued that with the "renormalized" Bernoulli formula for the pressure

$$p = -\frac{1}{2} \alpha \bar{v}^2 ; \quad (134)$$

$$\alpha \approx 0.95 \quad (135)$$

the Hopf chain of equations for the velocity moments $\langle (\Delta \vec{v} \cdot \hat{r})^n \rangle$ can be closed, providing relations for the multi-fractal exponents, closely matching those observed in numerical simulations.

As we know that the Bernoulli equation is not valid in a turbulent flow, this observation looks like a paradox.

However, in the CVS theory, these estimates make sense.

For the (majority of) points in space outside the vortex surface, the original Bernoulli formula, with $\alpha = 1$, holds. We reinterpret coefficient α as a probability of having no vorticity in a given point, involved in the computation of the Hopf moments.

The unconditional probability of avoiding a randomly translated and rotated smooth surface at a given point in space equals 1. However, there are several reasons for this probability α to be less than 1.

One is the finite thickness of the vortex sheet:

$$h \propto \sqrt{\frac{v}{\sigma}} \sim v^{\frac{3}{5}} \sim \text{Re}^{-\frac{1}{2}} \quad (136)$$

With $\text{Re} \sim 10^4$, this thickness measures in percents of the mean radius, which by itself can explain the 5% deviation from 1.

Another reason is that in the conditions used to compute the Hopf equations for the velocity moments, a vortex surface must be present between the two points \vec{r}_1, \vec{r}_2 . However, each of these two points belongs to the potential flow region.

The conditional probability of having a vortex sheet between two points would be finite, providing another source of renormalization of the Bernoulli law.

The arguments involved in²³ were relying on the turbulent viscosity notion, which we do not know how to justify in our theory. Still, the turbulent viscosity is an existing effect in the complementary approach with fluctuating velocity field. Perhaps, our effect of avoiding the vortex sheet is a dual description of the same phenomenon of turbulent viscosity.

The complete theory would have to compute the moments from the first principle. Then we will find the full function of two variables $n, \log |\Delta r|$, currently approximated by the multifractal scaling law.

3.5. Wilson Loop Statistics

Let us assume that we have some CVS surface parameterized by the random tensor $W = \text{diag}(a, b, c)$.

There are space translations, factored by a cylindrical translation in the z axis and parameters of the symmetric traceless matrix W : two eigenvalues $c > 0, a \in (-2c, -c/2)$ plus arbitrary rotations $\Omega \in S_2$ of the coordinate system.

As we described in the previous sections, we treat this W as the background uniform strain created by other vortex structures far away from the surface's axis. Thus, one would think that this strain, adding up strains from a large number of

randomly positioned vortex structures like this one, would be a random traceless symmetric tensor.

The z axis of the tube automatically aligns with the leading eigenvector of W , the one with the largest eigenvalue $c > 0$. The CVS stability requires this.

There remains an integral over zero modes: translation and rotation of the coordinate system plus two eigenvalues of the random constant strain at infinity. We should integrate over these parameters the observables computed for a particular solution of CVS.

To be specific, let us consider the loop average

$$W_C(\gamma) \propto \int d^3r_0 d\Omega dP(p, q) \exp\left(i\gamma \oint_C v_\alpha(\vec{r}) dr_\alpha\right) \quad (137)$$

The velocity circulation in the exponential comes only from the intersection points of the loop C with our cylindrical surface. A simple loop intersects the surface in two points or does not intersect at all, so we have

$$\Gamma_{12} = \oint_C v_\alpha dr_\alpha = \Gamma(\eta_2) - \Gamma(\eta_1) \quad (138)$$

Thus, up to extra terms independent of γ

$$W_C(\gamma) \propto \int d^3r_0 d\Omega dP(a, b) \Pi_S(\vec{r}_0, \Omega, \gamma) \quad (139)$$

The factor

$$\begin{aligned} \Pi_S(\vec{r}_0, \Omega, \gamma) &= \int_0^1 dl_1 |C'(l_1)| \int_0^1 dl_2 |C'(l_2)| \\ &\int_{\vec{r}_1 \in S} \int_{\vec{r}_2 \in S} \delta^3\left(\vec{r}_1 + \Omega \cdot (\vec{r}_0 - \vec{C}(l_1))\right) \delta^3\left(\vec{r}_2 + \Omega \cdot (\vec{r}_0 - \vec{C}(l_2))\right) \\ &\exp\left(i\gamma(\Gamma(\eta_2) - \Gamma(\eta_1))\right) \end{aligned} \quad (140)$$

was already computed in²⁴

$$\Pi_S(\vec{r}_0, \Omega, \gamma) = \frac{|\vec{\sigma}_1| |C'(l_1)|}{|\vec{\sigma}_1 \cdot \Omega \cdot \vec{C}'(l_1)|} \frac{|\vec{\sigma}_2| |C'(l_2)|}{|\vec{\sigma}_2 \cdot \Omega \cdot \vec{C}'(l_2)|} \theta(\vec{r}_1 \in S) \theta(\vec{r}_2 \in S)$$

$$\exp\left(i\gamma(\Gamma(\eta_2) - \Gamma(\eta_1))\right); \quad (141)$$

$$\vec{\sigma}_1 = \vec{\sigma}(\vec{r}_1); \vec{\sigma}_2 = \vec{\sigma}(\vec{r}_2); \quad (142)$$

$$\vec{r}_1 = \Omega \cdot (\vec{C}(l_1) - \vec{r}_0); \vec{r}_2 = \Omega \cdot (\vec{C}(l_2) - \vec{r}_0); \quad (143)$$

This integral depends on the geometry of the problem: the relation between the loop C and the cylinder. The phase factor depends on the random strain parameters via known $\Gamma(\eta)$.

We are left with an integral over $2d$ translations \vec{r}_0 against the cylinder's axis and the O_3 rotations Ω .

The two theta functions, restricting the points to be on the intersection of the surface and the loop, are zero if the point \vec{r}_0 moves from the surface farther than the maximal size of the loop C .

The integration region for \vec{r}_0 is some layer around the vortex surface, with the width equal to the maximal distance between two points on the loop.

The integration over rotations Ω is compact. Therefore, this integral looks like a relatively straightforward integral from a computational point of view.

As we already mentioned, there is no time-reversal symmetry that would reflect γ . Therefore, the flux $\Delta\Gamma$ is the same sign as q in our irreversible solution.

As a consequence, our Wilson loop will be a complex number. Unfortunately, nobody has measured it in DNS, but its Fourier transform (over the parameter γ , not over space coordinates) represents the circulation PDF measured with high accuracy.

This Fourier transform would simply mean replacement

$$\exp(i\gamma(\Gamma(\eta_2) - \Gamma(\eta_1))) \Rightarrow \delta\left((\Gamma(\eta_2) - \Gamma(\eta_1)) - \oint_C \vec{v} \cdot d\vec{r}\right) \quad (144)$$

This delta function is welcome, as it will reduce the dimension of the remaining integration over \vec{r}_0 .

After that, *Mathematica*[®] can compute this finite integral with arbitrary precision.

Another possibility is to compute the moments of the circulation $M_n = \langle (\oint_C \vec{v} \cdot d\vec{r})^n \rangle$ which would correspond to the replacement

$$\exp(i\gamma(\Gamma(\eta_2) - \Gamma(\eta_1))) \Rightarrow ((\Gamma(\eta_2) - \Gamma(\eta_1)))^n \quad (145)$$

Thus, there is a steep but clear path to compute a Wilson loop using the above formulas. There is much data in DNS regarding the distribution of the velocity circulation, which is related to a Fourier transformation of the Wilson loop.

It would be very interesting to finish this large computation and compare with the DNS data.

4. Discussion

The CVS theory offers an approach to turbulence that one can study analytically and numerically.

Let us remind and discuss the general ideas behind this theory.

We are trying to solve the Navier-Stokes equations for an infinite time evolution, given that the laminar flow is unstable. This unstable solution could cover the whole phase space of the fluid mechanics; however, we suspect that there are some low-dimensional attractors in that space. The solution would cover the subspace of these attractors like the Newtonian dynamics covers the energy surface in ergodic motion.

We also know the phenomenon of anomalous dissipation: the dissipation in extreme turbulence occurs in the regions of high vorticity, which compensates for the viscosity factor in front of the enstrophy integral.

Furthermore, we conjecture that these regions of high vorticity are vortex surfaces. There are several reasons to believe so, both theoretical and (numerical or real) experimental sides.

The Hamiltonian dynamics of vortex surfaces^{19,20} can be solved exactly in some important cases, and the resulting solutions have all nice properties, including anomalous dissipation.

We have found in our previous work^{24,25} that the steady-state of the vortex surface is a promising candidate for such an attractor in phase space. At first sight, it appears that these steady vortex surfaces have some local degrees of freedom, corresponding to the arbitrary shape of the surface, as long as the velocity gap satisfies certain integral equations, following from the minimization of the Hamiltonian.

Initially, we speculated that these surface degrees of freedom were described by some version of a solvable string theory.²⁴ There are two kinds of surface degrees of freedom: the surface shape and the internal metric on this surface, described by the Liouville field.

In fluid dynamics terms, the fluctuations of this internal metric correspond to the tangent motions of the fluid, equivalent to the reparametrization of this surface.

The shape of the surface was assumed frozen in the turbulent flow in,²⁴ and the remaining internal metric was assumed to be responsible for the multifractal scaling laws for the moments of velocity circulation.

The new recent understanding eliminated the shape of the surface as degrees of freedom while placing no restrictions on the internal metric on this surface.

Some surfaces are "more equal" than others because they are stable at the microscopic level. These are the CVS surfaces satisfying the stability equations (1).

It is truly remarkable that such a simple equation, involving just three letters, leads to so many specific consequences for the turbulent flow.

The negative normal strain presses vorticity into the CVS surface from both sides, leading to a narrow Gaussian profile of vorticity in the normal direction. The width of this boundary layer goes to zero as some negative power of Reynolds number in the turbulent limit.

We assume that our flow and the surface are subject to a background strain, a random traceless matrix adding up from Biot-Savart tails of many other vortex structures located far away from this one. Such random strain is described by eigenvalues a, b, c adding up to zero. The parameters a, b, c obey a Gaussian distribution multiplied by a famous Vandermonde determinant.

The normal strain is uniform all around our vortex surface $S_{nn} = -c$, so that we have one of the stability criteria fulfilled if the axis of the vortex tube points along the main eigenvector of the strain, with a positive eigenvalue c . The tangent strain is degenerate: there is zero strain along the tangent velocity gap.

The energy dissipation occurs at the surface, and we have demonstrated¹⁰ that

this surface integral is conserved in the Navier-Stokes dynamics in the turbulent limit.

Let us stop and think about this conservation law. It is *not* an Euler conservation law, violated by viscosity, like the energy conservation. Instead, we have found a previously unknown Navier-Stokes conservation law, and it comes about as a result of the exact cancellation of the advection, vortex stretching, and diffusion terms in the Navier-Stokes equation used for the time derivative of the enstrophy.

The Euler dynamics would lead to an explosion or decay of enstrophy were it not offset by the diffusion in full Navier-Stokes equation. For any other vortex surface but the CVS the diffusion would not cancel the vortex stretching so that the notorious energy dissipation constant \mathcal{E} would not be constant.

The Kolmogorov theory kept this paradox unresolved for 80 years. The basic constant of the theory was constant with one definition (three-point function of velocity), but not with an alternative one (enstrophy), and nobody knew why.

As we see it now, \mathcal{E} is conserved because of the CVS stability of the vortex surfaces hidden behind the rough picture of the energy flow in Fourier space. One cannot describe the shape of the discontinuity surface by a finite (or even convergent) set of Fourier coefficients of the velocity field – it is like describing Mona Lisa's smile by the spectral analysis of color pixels of the Leonardo painting.

True, the energy flows from large scales to small scales in our theory. It dissipates at small scales in thin boundary layers of the CVS surface, but this spatial picture is different from the hierarchical cascade of energy "from a big eddy to a smaller one."

The only way to reconcile these two pictures is to assume the Russian doll of nested tubes, passing the energy from the outer tube to the inner ones, with each tube dissipating energy as discussed above. Someone still has to find such a solution of the CVS equations.

The conservation of energy dissipation on the CVS surface makes this parameter \mathcal{E} an appropriate scaling factor for the K41 theory viewed as dimensional analysis, which describes the medium Reynolds numbers so well.

Let us come back to our cylindrical solution.

This solution describes a vortex tube much larger than the viscous scale. All vorticity collapses to the boundary layer; this layer's width will decrease as a positive viscosity power in the turbulent limit.

The flow is, therefore, potential both inside and outside. The normal velocity vanishes on both sides of the surface of the tube, but the tangent velocity is finite, and there is a tangent gap.

Hollow vortex tubes were observed in the recent DNS,² but it is hard to tell until some research would specifically hunt for hollow tubes in turbulent flow simulations.

The uniform strain tensor, distributed as a Gaussian random traceless matrix, is forcing our flow.

The origin of this random force is the accumulation of a large number of $1/R^3$ tails of the Biot-Savart laws for other remote vortex tubes with random locations and random orientations.

The stability condition $S_{nn} < 0$, coming from the microscopic analysis of the Navier-Stokes equation in a boundary layer, fixes the sign of the flow.

The same requirement follows from the Kelvin-Helmholtz stability of the vortex surface against the low wave-length perturbations. The high wave-length perturbations of the sharp vortex surface are always unstable, but presumably, viscous diffusion stabilizes those perturbations. At least this happens so in the Burgers-Townsend solution, which applies to our vortex surface in a local tangent plane at any smooth part of the tube.

This stability condition is the origin of the flow's irreversibility. We choose the parameters so that the energy dissipation (and equal energy pumping) stays finite in the limit of vanishing viscosity.

We considered these closed vortex surfaces (vortex tubes) as a dilute gas, with a large mean distance between tubes, compared to their size.

In this dilute gas approximation, we derived the Gaussian random strain from an infinite number of remote vortex structures, adding to the Biot-Savart formula for the strain at large distances and averaging to the random constant stress tensor due to the Central Limit theorem.

This calculation leads to a self-consistency relation (127) for the mean distance \bar{R} between vortex tubes, their length L , and the perimeter $|C|$ of the cross-section loop.

The perimeter being much smaller than the mean distance between the vortex tubes vindicates the underlying assumption of an ideal gas of vortex tubes.

The statistical distribution of the perimeter $|C|$, following from the Gaussian distribution of the background strain, offers the microscopic explanation for the "multifractal" scaling laws for the moments of velocity difference.

Our estimate (128) provides the mechanism for the multifractal law, although not yet allowing us to compute the anomalous dimension index $\zeta(n)$.

Moreover, the moments of velocity difference would likely be a more complex function of $n, |\Delta r|$ than just $|\Delta r|^{\zeta(n)}$, which could be approximated by the power laws at specific integer values of n . This unknown function remains an open problem for future study in the CVS theory.

The SY phenomenological theory²³ relies on the postulate of the renormalized Bernoulli law for local values of pressure in the turbulent flow. We interpret this renormalized law $p = -\frac{1}{2}\alpha\bar{v}^2$ as a probability α to have no vorticity in the point under study times the local pressure in a potential flow.

The velocity differences in the piecewise potential flow can be singular: the vortex tube's surface separates the pair of points with a certain probability.

In this case, the pressure obeys the Bernoulli formula on each side. The velocity difference is dominated by the tangent velocity gap, scaling as some power of the

size of the CVS surface. The size has an approximately multifractal distribution, which may lead to the desired scaling law.

This topological observation resolves the paradox of singular velocity moments in the potential flow of.²³ With this interpretation, the multifractal law is not exact – it is only an approximation to the future microscopic theory.

Using the dilute gas approximation, we computed the PDF for the perimeter of the tube cross-section, plotted in log-log scale at 12. This curve is universal in our solution; there are no model approximations nor any dimensionless parameters.

In the same way, one can compute the distribution of the circulation and other observables, such as the Wilson loop $\left\langle \exp \left(i \gamma \oint_C v_\alpha dr_\alpha \right) \right\rangle$.

5. Summary

- *Attractor* in the Navier-Stokes equation is found: vortex tubes with singular shape, parametrized by the Gaussian random symmetric traceless matrix (88) in addition to random 3D location and random scale.
- *Analytical Solution* is presented for the flow (55), (59), (64). Far away from the tubes, there is a potential flow with random uniform background strain.
- *Irreversibility* follows from the inequality on the local normal strain at the vortex tube: $S_{nn} < 0$. This inequality is required for microscopic stability.
- *Enstrophy* is conserved as a consequence of the stability equation: $\hat{S} \cdot \Delta \vec{v} = 0$.
- *Stochasticity* is explained by the accumulation of contributions to the background strain from large number of uncorrelated remote vortex tubes via Biot-Savart law (85).
- *Multifractals* could be imitated by fluctuations (105) of the shape and perimeter of the CVS solution.

Acknowledgments

I am grateful to Theo Drivas, Dennis Sullivan, Katepalli Sreenivasan, Victor Yakhot, and the Stony Brook University Einstein seminar participants for stimulating discussions of this work. The help from Arthur Migdal with *Mathematica*[®] is also greatly appreciated.

This work is supported by a Simons Foundation award ID 686282 at NYU.

Appendix A. The Cylindrical CVS equations

Let us re-derive the cylindrical CVS equations of¹⁰ without unnecessary assumption of real and equal functions $d\Gamma_\pm$ in (19).

The normal vector in complex notation

$$\sigma = i C'(\theta) \tag{A.1}$$

The normal projection of velocity field

$$v_x\sigma_x + v_y\sigma_y = \mathbf{Re} (v_x - i v_y)\sigma = \frac{\mathbf{Im} \left((v_x - i v_y)C'(\theta) \right)}{|C'(\theta)|} \quad (\text{A.2})$$

The first CVS equation (vanishing normal velocity on each side) becomes

$$\mathbf{Im} \left(V_{\pm}(C(\theta))C'(\theta) \right) = 0; \forall \theta \quad (\text{A.3})$$

The second and third CVS equations require the computation of the strain related to the complex velocity $F_{\pm} = \phi'_{\pm}$. The strain on each side is a 3×3 matrix

$$\hat{S}_{\pm}(\eta) = \begin{pmatrix} \mathbf{Re} F'_{\pm}(\eta) + a & -\mathbf{Im} F'_{\pm}(\eta) & 0 \\ -\mathbf{Im} F'_{\pm}(\eta) & -\mathbf{Re} F'_{\pm}(\eta) + b & 0 \\ 0 & 0 & c \end{pmatrix} \quad (\text{A.4})$$

Let us introduce notations

$$F(\eta) = \frac{1}{2}(F_+(\eta) + F_-(\eta)); \quad (\text{A.5})$$

$$\Delta F(\eta) = F_+(\eta) - F_-(\eta); \quad (\text{A.6})$$

$$p = (a + b)/2; \quad (\text{A.7})$$

$$q = (a - b)/2 \quad (\text{A.8})$$

The null vector equation $(\hat{S}_+(\eta) + \hat{S}_-(\eta)) \cdot \Delta \vec{v} = 0$ provides the following complex equation

$$\Delta F^*(\eta)(F'(\eta) + q) + p\Delta F(\eta) = 0; \forall \eta \in \mathbb{C}; \quad (\text{A.9})$$

The product

$$\Gamma(\theta) = C'(\theta)\Delta F(C(\theta)) \quad (\text{A.10})$$

is real, in virtue of the Neumann boundary conditions. The difference of the two Neumann equations (A.3) reduces to $\mathbf{Im} \Gamma = 0$.

Thus, multiplying (A.9) by $C'(\theta)C'^*(\theta)$ and using the fact that $\Gamma(\theta)$ is real we find

$$C'(\theta) \left(F'(C(\theta)) + q \right) + pC'^*(\theta) = 0; \forall \eta \in \mathbb{C}; \quad (\text{A.11})$$

This equation is simpler than it looks: it is reduced to the total derivative.

$$\frac{d}{d\theta} (F(C(\theta)) + qC(\theta) + pC^*(\theta)) = 0 \quad (\text{A.12})$$

The generic solution is

$$F(C(\theta)) + qC(\theta) + pC^*(\theta) = A \quad (\text{A.13})$$

with some complex constant A .

Plugging it back to the (A.3) we have everything cancel except one term

$$\mathbf{Im} \left(AC'(\theta) \right) = 0; \forall \eta = C(\xi) \quad (\text{A.14})$$

The nontrivial solution for $C(\theta)$ would correspond to $A = 0$.
This solution is equivalent to the equation (25) we stated in the text.

Appendix B. Unbounded Solutions of the Cylindrical CVS Equations

In this section, we describe some unbounded solutions of the cylindrical CVS equations (30). Though these solutions are not physical, in our judgment, we present them for completeness of the mathematical analysis. Maybe there are some special situations where these solutions will display themselves in the turbulent flow.

In this section we use another index $\alpha = \gamma + \frac{1}{2}$.

Appendix B.1. Parabolic curves

Let us consider positive α first (the parabolic curves).

This solution passes through the origin and it will have no singularity at $\tau = 0$ in case $\alpha = \frac{1}{2} + n, n \in \mathbb{Z}, n \geq 0$.

The case $n = 0$ corresponds to a tilted straight line, Fig.13. This is just a Burgers-Townsend planar vortex sheet. The next cases are already nontrivial Fig.14,15,16.

However, not all positive n are acceptable. For even positive n we have a cusp in a curve, because only positive $r(\theta)$ exist at $\theta \rightarrow 0$. This is clearly visible at $n = 2$ (Fig.15).

For odd positive $n = 2k + 1$ there is a linear relation between x, y at small τ provided $\beta \neq 0$. The slope of the curve $y(x)$ at $x = \pm 0$ is the same.

Higher derivatives are singular, as we have

$$x \sim \tau^{2k+1} \cos(\beta) (1 - \tan(\beta) \tau); \quad (\text{B.1})$$

$$y \sim \tau^{2k+1} \sin(\beta) (1 + \cot(\beta) \tau); \quad (\text{B.2})$$

$$y \rightarrow \tan(\beta) x \left(1 + \frac{2 \operatorname{sign} x}{\sin \beta} \left(\frac{|x|}{\cos(\beta)} \right)^{\frac{1}{2k+1}} \right); \quad (\text{B.3})$$

$$\frac{dy}{dx} \rightarrow \tan(\beta) \text{ at } x \rightarrow \pm 0 \quad (\text{B.4})$$

As the slopes $\frac{dy}{dx}$ are the same at $x = \pm 0$, the vortex sheet reduces to a plane up to higher-order terms. Thus, the Burgers-Townsend solution, assuming the infinitesimal thickness of the vorticity layer, will still apply here. Ergo, the sheet will be stable at this point and the rest of the surface.

Thus, we have found the discrete parametric family of CVS shapes. It simplifies in terms of $\tau = \tan \theta$.

$$\eta(\tau) = e^{i\beta} (1 + i\tau) \tau^{2k+1}; \quad (\text{B.5})$$

$$k \in \mathbb{Z}, k \geq 0; \quad (\text{B.6})$$

$$-\infty < \tau < \infty; \quad (\text{B.7})$$

We have a conformal map from the τ plane to the plane of $\eta = x + iy$, with our curve C corresponding to the real axis. The physical region outside the loop corresponds to the sector in the lower semiplane, $-\frac{\pi}{(k+1)} < \arg \tau < 0$.

The infinity in the physical space corresponds to infinity in the τ plane.

There are two singular points corresponding to the vanishing derivative $\eta'(\tau) = 0$. This happens at

$$\tau = 0; \quad (\text{B.8})$$

$$\tau = \frac{i(2k+1)}{2(k+1)}; \quad (\text{B.9})$$

The first one maps to the origin in the η plane. The second one is in the upper τ semiplane, so it does not affect the inverse function $\tau(\eta)$ in the physical sector of the lower semiplane.

The next step is to find the holomorphic function $F_+(\eta)$ which defines the complex velocity on the external side of the sheet (the internal side has linear velocity $F_-(\eta) = (p + iq)\eta$).

From the CVS equation we get the boundary values, which we express in terms of η, η^*

$$F_+(\eta) = -(p + a - b + iq)\eta + c\eta^*; \quad \forall \eta \in C \quad (\text{B.10})$$

We have to continue this function from the curve (B.5) into the part of the complex plane outside of this curve.

Let us express the right side in terms of τ

$$f(\tau) = -(p + a - b + iq)\eta(\tau) + c\tilde{\eta}(\tau) \quad (\text{B.11})$$

Here $\tilde{\eta}(\tau)$ is the complex conjugate expression for η

$$\tilde{\eta}(\tau) = e^{-i\beta} (1 - i\tau) \tau^{2k+1}; \quad (\text{B.12})$$

$$(\text{B.13})$$

At the real axis of τ the variables $\eta(\tau), \tilde{\eta}(\tau)$ will be complex conjugates, and the boundary value

$$f(\tau) = F_+(\eta(\tau)); \quad \forall \text{Im } \tau = 0 \quad (\text{B.14})$$

Now we have an obvious analytic continuation to the lower semiplane of τ . After some algebra we get¹⁵

$$\eta(\tau) = e^{i\beta} (1 + i\tau) \tau^{2k+1}; \quad (\text{B.15})$$

$$f(\tau) = -ie^{-i\beta} \frac{\tau^{2k+1}}{2(4k+3)} \left(c((8k+7)\tau + 8k+5) + e^{i\beta}(4k+3)(\tau - i)(2a+c) \right) \quad (\text{B.16})$$

This parametric function in the sector $-\frac{\pi}{(k+1)} < \arg \tau < 0$ of the complex τ plane represents an implicit solution of the CVS equation.

Now, let us consider the limit $\tau \rightarrow \infty$ corresponding to $\eta \rightarrow \infty$. In this limit, the function $F_+(\eta(\tau))$ linearly grows

$$F_+(\eta) \rightarrow B\eta; \quad (\text{B.17})$$

$$B = -a - \frac{1}{2}c \left(1 + \frac{e^{-i\beta}(8k+7)}{4k+3} \right) \quad (\text{B.18})$$

This means that the true value of the xy components of strain at infinity is not $\text{diag}(a, -c - a)$ we thought it was. It is instead

$$\hat{S} = \begin{pmatrix} -\frac{c((8k+7)\cos(\beta)+4k+3)}{8k+6} & -\frac{c(8k+7)\sin(\beta)}{8k+6} \\ -\frac{c(8k+7)\sin(\beta)}{8k+6} & \frac{c(8k+7)\cos(\beta)-c(4k+3)}{8k+6} \end{pmatrix} \quad (\text{B.19})$$

The eigenvalues of this strain are

$$\left\{ -\frac{c(6k+5)}{4k+3}, \frac{2c(k+1)}{4k+3} \right\} \quad (\text{B.20})$$

Note that the angle β dropped from the eigenvalues. This angle can be eliminated by the $U(1)$ transformation $\eta \rightarrow \eta e^{-i\beta}$, which leaves the eigenvalues invariant.

The parabolic solution does not decrease at infinity, so it is inadequate for the turbulent statistics we develop later in this paper.

Appendix B.2. Hyperbolic curves

Let us now consider the hyperbolic curves with negative $\alpha < -\frac{1}{2}$, which do not need to be half-integer. We redefine our parameters as follows:

$$\eta(\zeta) = \pm e^{i\beta} \left(\zeta + i\zeta^{-\mu} \right); \quad (\text{B.21})$$

$$\zeta = \tau^{\alpha - \frac{1}{2}}; \quad (\text{B.22})$$

$$\mu = \frac{1+2\alpha}{1-2\alpha}; \mu > 0; \quad (\text{B.23})$$

$$0 < \zeta < \infty \quad (\text{B.24})$$

The two curves on Fig. 17, 18 correspond to various μ, β . Note that there are no singularities at the origin, as both curves are going around it.

There is a singularity of the inverse function at the point in the upper semiplane: where $\eta'(\zeta_0) = 0$:

$$\zeta_0 = (i\mu)^{\frac{1}{\mu+1}} \quad (\text{B.25})$$

Therefore, we need to use the lower semiplane as a physical domain for $f(\zeta) = F_+(\eta(\zeta))$.

The holomorphic function $f(\xi)$ is reconstructed by means of the same steps as in the parabolic case. We get

$$f(\xi) = \frac{1}{2}e^{-\frac{1}{2}(i\beta)\xi} \xi \left(\frac{c(\mu-3)}{\mu-1} - e^{i\beta}(2a+c) \right) - \frac{ie^{-\frac{1}{2}(i\beta)\xi} \xi^{-\mu} \left(c(3\mu-1) + e^{i\beta}(\mu-1)(2a+c) \right)}{2(\mu-1)} \quad (\text{B.26})$$

Let us now find the limit at $\xi \rightarrow \infty$, when η and f both linearly grow

$$f \rightarrow \eta B; \quad (\text{B.27})$$

$$B = -a + \frac{1}{2}c \left(-1 + \frac{e^{-i\beta}(\mu-3)}{\mu-1} \right) \quad (\text{B.28})$$

We want this coefficient to be zero so that $f(\eta)$ decreases at infinity. The solution of this complex equation for β, μ is

$$\begin{cases} \beta = 0; & \mu = 1 - \frac{c}{a}; \\ \beta = \pi; & \mu = 1 - \frac{c}{b}; \end{cases} \quad (\text{B.29})$$

From the inequalities between the three eigenvalues $a < b < c$ adding to zero, we get

$$-2c < a < -\frac{c}{2}; \quad (\text{B.30})$$

$$-\frac{c}{2} < b < c; \quad (\text{B.31})$$

which makes this index μ limited to the interval

$$\begin{cases} \beta = 0; & \frac{3}{2} < \mu < 3; \\ \beta = \pi; & -\infty < \mu < \infty; \end{cases} \quad (\text{B.32})$$

We choose the first solution, as in this case, μ varies in the positive region where there are no singularities.

Now, we observe that at $\beta = 0, \pi$, which means $q = 0$ there is an extra symmetry in the equation (30)

$$C \Rightarrow C^* \quad (\text{B.33})$$

This means that now all four branches of the hyperbola

$$|y||x|^\mu = \text{const}; \quad (\text{B.34})$$

are the parts of a single periodic solution $C(\theta)$ (Fig 19).

These four branches define the domain inside the loop C where the holomorphic velocity

$$F_-(\eta) = -2a\eta; \quad (\text{B.35})$$

As for the function F_+ it is just a negative power

$$F_+ \left(x \pm i |x|^{-\mu} \right) = +2i c |x|^{-\mu}; \quad (\text{B.36})$$

The loop $C(\theta)$ defined by these four branches is a periodic function, with singularities at $\theta = k\pi/2$.

Topologically, on a Riemann sphere, these four branches divide the sphere into five regions. There is an inside region, with the boundary touching Riemann infinity four times.

Each of the four remaining outside regions is bounded by hyperbola, starting and ending at infinity. (Fig. 20).

Let us consider the lower right hyperbola with $y = -x^{-\mu}, x > 0$

The values of $F_+(\eta)$ in three other external regions will be obtained from this one by reflection against x or y axis.

$$F_+(-\eta) = -F_+(\eta); \quad (\text{B.37})$$

$$F_+(\eta^*) = F_+^*(\eta); \quad (\text{B.38})$$

We can continue the above parametric equation for the function f to the complex plane for the variable w , with the cut from $-\infty$ to 0. The phase of the multivalued function $w^{-\mu}$ is set to $\arg w^{-\mu} = 0, w > 0$.

$$\eta = w - i w^{-\mu}; \quad (\text{B.39})$$

$$F_+ = 2i c w^{-\mu}; \quad (\text{B.40})$$

This parametric function has a square root singularity at the point where derivative $\partial_w \eta = 1 + i \mu w^{-\mu-1}$ vanishes:

$$w_c = (-i \mu)^{\frac{1}{\mu+1}} \quad (\text{B.41})$$

For positive μ , this singularity is located in the lower semiplane of w , leaving the upper semiplane as a physical domain.

We have drawn the complex maps of the derivative $\partial_w \eta = 1 + i \mu w^{-\mu-1}$ for $\mu = 1.51, 2, 2.99$ (Fig. 21,22,23). We indicate the zeros of $\partial_w \eta$ as holes on the surface (white circles).

To check whether these singularities penetrate the physical region, we have drawn in black the boundaries of the physical regions

$$\mathbf{Re} \eta^\mu \mathbf{Im} \eta = \pm 1 \quad (\text{B.42})$$

We observe that these square root singularities lie outside the physical region. This physical region is above the black line in the first quadrant, and there are no singular points there.

Inside the tube, the velocity is linear, and an extra linear term $F_-(\eta) = -2a\eta$; is potential, so that the incompressibility is preserved

$$V^- = ax - i by - 2a(x + iy) = -ax + i(c - a)y \quad (\text{B.43})$$

To summarize, the velocity field $\vec{v}(x, y, z)$ and complex coordinates $\eta = x + iy$ are parametrized as a function of a complex variable w as follows (with extra scale factor R_0 included in the solution $C(\theta)$ of the scale invariant equation (30))

$$v_z = cz; \quad (\text{B.44})$$

$$v_x - iv_y = ax - iby + F_{\pm} \left(\frac{x + iy}{R_0} \right); \quad (\text{B.45})$$

$$F_-(\eta) = -2a\eta; \quad (\text{B.46})$$

$$F_+(\eta) = 2icw(\eta)^{-\mu}; \quad \mathbf{Re} \eta > 0, \mathbf{Im} \eta < 0; \quad (\text{B.47})$$

$$F_+(-\eta) = -F_+(\eta); F_+(\eta^*) = F_+(\eta); \quad (\text{B.48})$$

$$w(\eta) : \eta = w - iw^{-\mu}; \quad (\text{B.49})$$

$$C : |x|^\mu |y| = R_0^{1+\mu}; \quad (\text{B.50})$$

$$\mu = 1 - \frac{c}{a}; \quad \frac{3}{2} < \mu < 3; \quad (\text{B.51})$$

$$\Delta\Gamma = \oint_C \vec{v}(\vec{r}) d\vec{r} = 0; \quad (\text{B.52})$$

We show in Fig. 24, 25 the streamline plot of this flow in the xy plane. We performed analytical and numerical computations in.²⁶

While computing the complex velocity and coordinates using parametric equations, we restricted w to the physical region and populated this region by an irregular grid in angular variables in the w plane.

After that we used *ListStreamPlot* method of *Mathematica*[®].

The grid resolution does not allow tracking the boundary's immediate vicinity, but we computed the normal velocity numerically at the boundary. It turned out less than 10^{-15} on both sides of the sheet.

Appendix C. Symmetric Traceless Random Matrices

Let us investigate the general properties of the measure (86). First, the trace of the matrix is invariant with respect to orthogonal transformations

$$W \Rightarrow O^T \cdot W \cdot O; \quad (\text{C.1})$$

$$O^T = O^{-1}; \quad (\text{C.2})$$

$$\text{tr} W \Rightarrow \text{tr} W \quad (\text{C.3})$$

therefore this measure stays $O(n)$ invariant after insertion of the delta function of the trace.

The mean value of $\text{tr} W^2$ can be computed by the following method. Consider the normalization integral

$$Z_n(\sigma) = \int dP_\sigma(W) \quad (\text{C.4})$$

By rescaling the matrix elements $W_{ij} = \sigma w_{ij}$ we find the property

$$Z_n(\sigma) = \sigma^{\frac{(n+2)(n-1)}{2}} Z_n(1) \quad (\text{C.5})$$

Taking the logarithmic derivative of the original integral we get the identity

$$\frac{\sigma Z'_n(\sigma)}{Z_n(\sigma)} = \frac{\int dP_\sigma(W) \text{tr} W^2}{\sigma^2 Z_n(\sigma)} = \frac{\langle \text{tr} W^2 \rangle}{\sigma^2} \quad (\text{C.6})$$

On the other hand, taking the logarithmic derivative from (C.5) we find

$$\frac{\sigma Z'_n(\sigma)}{Z_n(\sigma)} = \frac{(n+2)(n-1)}{2} \quad (\text{C.7})$$

This formula produces the trace relation (87) in the text.

Higher moments of various products of matrix elements are also calculable analytically. We are studying these moments, and the generation function in.²⁷

References

1. T. Ishihara, T. Gotoh and Y. Kaneda, *Annual Review of Fluid Mechanics* **41**, 165 (12 2008), doi:10.1146/annurev.fluid.010908.165203.
2. D. Buaria, A. Pumir, E. Bodenschatz and P. K. Yeung, *New Journal of Physics* **21**, 043004 (Apr 2019), doi:10.1088/1367-2630/abo756.
3. K. P. Iyer, K. R. Sreenivasan and P. K. Yeung, *Phys. Rev. X* **9**, 041006 (Oct 2019), doi:10.1103/PhysRevX.9.041006.
4. A. Migdal, Analytic and numerical study of navier-stokes loop equation in turbulence (2019), [arXiv:1908.01422v1](https://arxiv.org/abs/1908.01422v1).
5. A. Migdal, Loop equation and area law in turbulence, in *Quantum Field Theory and String Theory*, eds. L. Baulieu, V. Dotsenko, V. Kazakov and P. Windey (Springer US, 1995) pp. 193–231.
6. G. Apolinario, L. Moriconi, R. Pereira and V. valadão, *PHYSICAL REVIEW E* **102**, 041102 (10 2020), doi:10.1103/PhysRevE.102.041102.
7. N. P. Müller, J. I. Polanco and G. Krstulovic, *Phys. Rev. X* **11**, 011053 (Mar 2021), doi:10.1103/PhysRevX.11.011053.
8. J. Burgers, A mathematical model illustrating the theory of turbulence, in *Advances in Applied Mechanics*, eds. R. Von Mises and T. Von Kármán (Elsevier, 1948) pp. 171 – 199.
9. A. A. Townsend, *Proc. Roy. Soc. Lond. Ser. A.* **208(1095)**, 534–542 (1951), doi:10.1098/rspa.1951.0179.
10. A. Migdal, Confined vortex surface and irreversibility. 1. properties of exact solution (2021), [arXiv:2103.02065v1](https://arxiv.org/abs/2103.02065v1) [physics.flu-dyn].
11. A. Migdal, *Physics of Fluids* **33**, 035127 (2021), <https://doi.org/10.1063/5.0044724>, doi:10.1063/5.0044724.
12. K. Shariff and G. E. Elsinga, *Physics of Fluids* **33**, 033611 (2021), <https://doi.org/10.1063/5.0045243>, doi:10.1063/5.0045243.
13. A. Migdal, General vortex sheet <https://www.wolframcloud.com/obj/sasha.migdal/Published/GeneralVortexSheet.nb> (August, 2021).
14. Wikipedia, Double layer (surface science) — Wikipedia, the free encyclopedia (2021), [Online; accessed 24-January-2021].

15. A. Migdal, Algebraic cvs <https://www.wolframcloud.com/obj/sasha.migdal/Published/AlgebraicCVS.nb> (August, 2021).
16. A. Migdal, Closed cvs <https://www.wolframcloud.com/obj/sasha.migdal.gmail/Published/ClosedCVS.nb> (October, 2021).
17. V. Falkner and S. Skan, *The London, Edinburgh, and Dublin Philosophical Magazine and Journal of Science* **12**, 865 (1931), <https://doi.org/10.1080/14786443109461870>, doi: 10.1080/14786443109461870.
18. Wikipedia, Falkner-Skan Boundary layer — Wikipedia, the free encyclopedia (2020), [Online; accessed 29-October-2020].
19. A. A. Migdal, Random surfaces and turbulence, in *Proceedings of the International Workshop on Plasma Theory and Nonlinear and Turbulent Processes in Physics, Kiev, April 1987*, ed. V. G. Bar'yakhtar (World Scientific, 1988), p. 460.
20. M. E. Agishtein and A. A. Migdal, *Physica D: Nonlinear Phenomena* **40**, 91 (1989), doi: [https://doi.org/10.1016/0167-2789\(89\)90029-8](https://doi.org/10.1016/0167-2789(89)90029-8).
21. Wikipedia, Random Matrix https://en.wikipedia.org/wiki/Random_matrix, (2021), [Online; accessed 30-September-2021].
22. A. Migdal, N dimensional tensor algebra and gradients <https://www.wolframcloud.com/obj/sasha.migdal/Published/NDimensionalTensorMath.nb> (Mar, 2021).
23. K. R. Sreenivasan and V. Yakhot, Dynamics of three-dimensional turbulence from navier-stokes equations (2021).
24. A. Migdal, *International Journal of Modern Physics A* **36**, 2150062 (2021), <https://doi.org/10.1142/S0217751X21500627>, doi:10.1142/S0217751X21500627.
25. A. Migdal, *International Journal of Modern Physics A* **35**, 2030018 (November 2020), arXiv:2007.12468v7 [hep-th], doi:10.1142/s0217751x20300185.
26. A. Migdal, Hyperbolic flow <https://www.wolframcloud.com/obj/sasha.migdal/Published/HyperbolicFlow.nb> (August, 2021).
27. A. Migdal, Matrix integrals <https://www.wolframcloud.com/obj/sasha.migdal/Published/MatrixIntegrals.nb> (May, 2021).

Appendix D. Figures

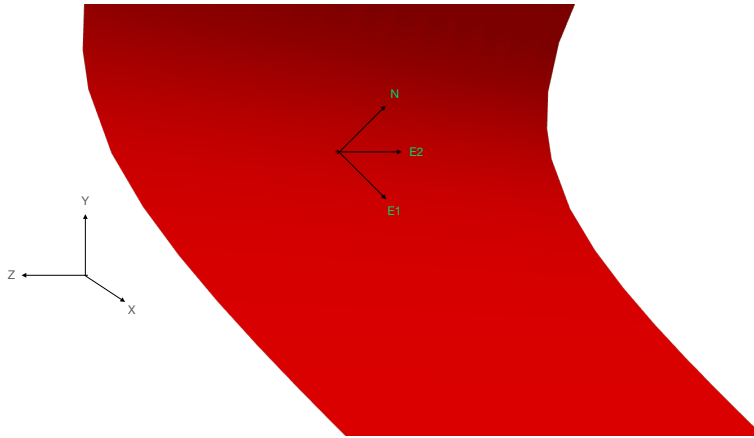


Fig. 1. The local tangent plane E_1, E_2, N and the global Cartesian frame X, Y, Z .

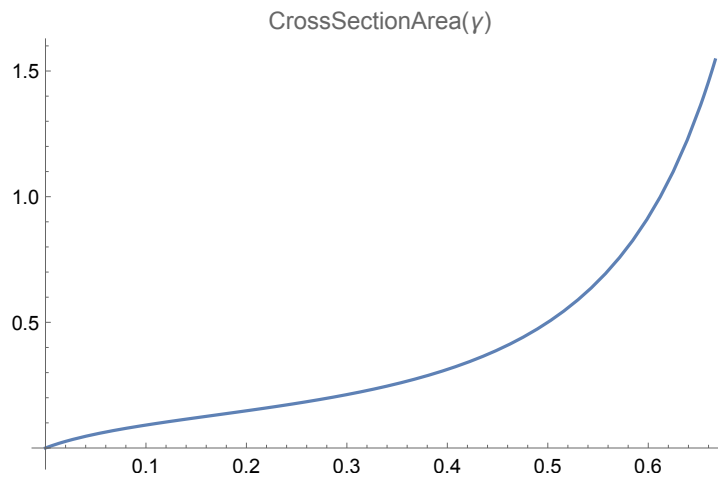


Fig. 2. Area inside the loop as a function of γ

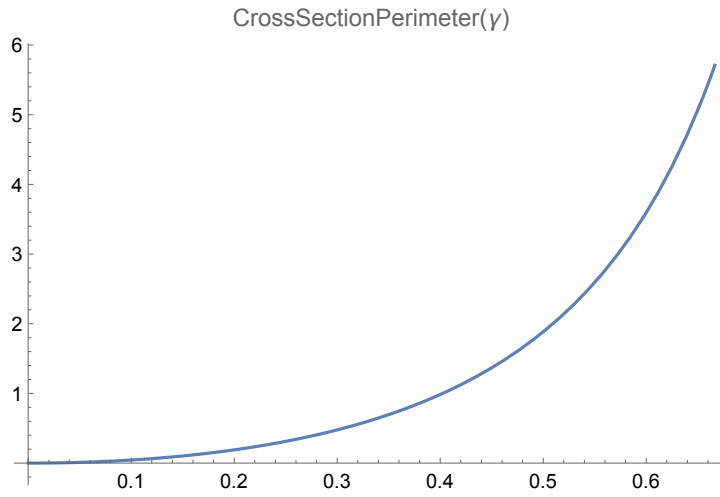


Fig. 3. Perimeter of the loop as a function of γ

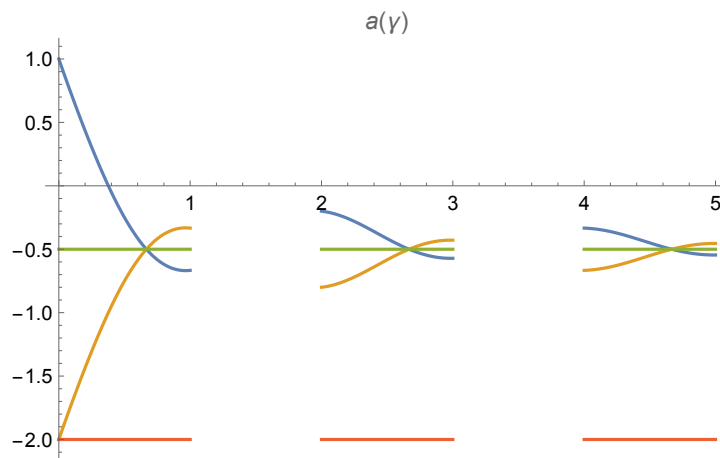


Fig. 4. Two branches of solution for $a(\gamma)/c$. The blue line corresponds to a_0 with $\beta = -\frac{1}{2}\pi\gamma$. The orange line corresponds to a_1 , with $\beta = \frac{1}{2}\pi(1-\gamma)$. The branches cross at the phase transition points $\gamma = \frac{2}{3} \bmod 2$.

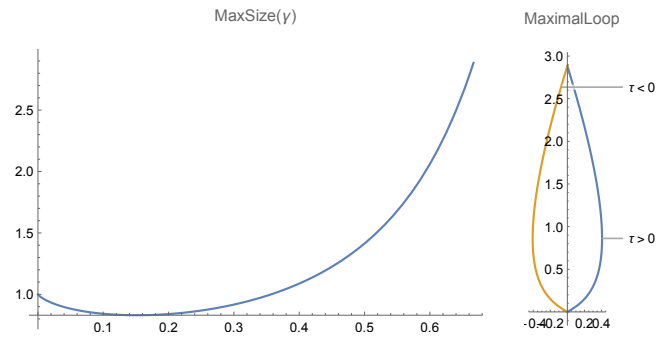


Fig. 5. Left: the height of the loop as a function of γ in the first stable region $0 < \gamma < 1$. Right: the shape of the maximal loop (for $\gamma = \frac{2}{3}, \beta = \frac{\pi}{3}$).

$$\gamma = \frac{1}{3}$$

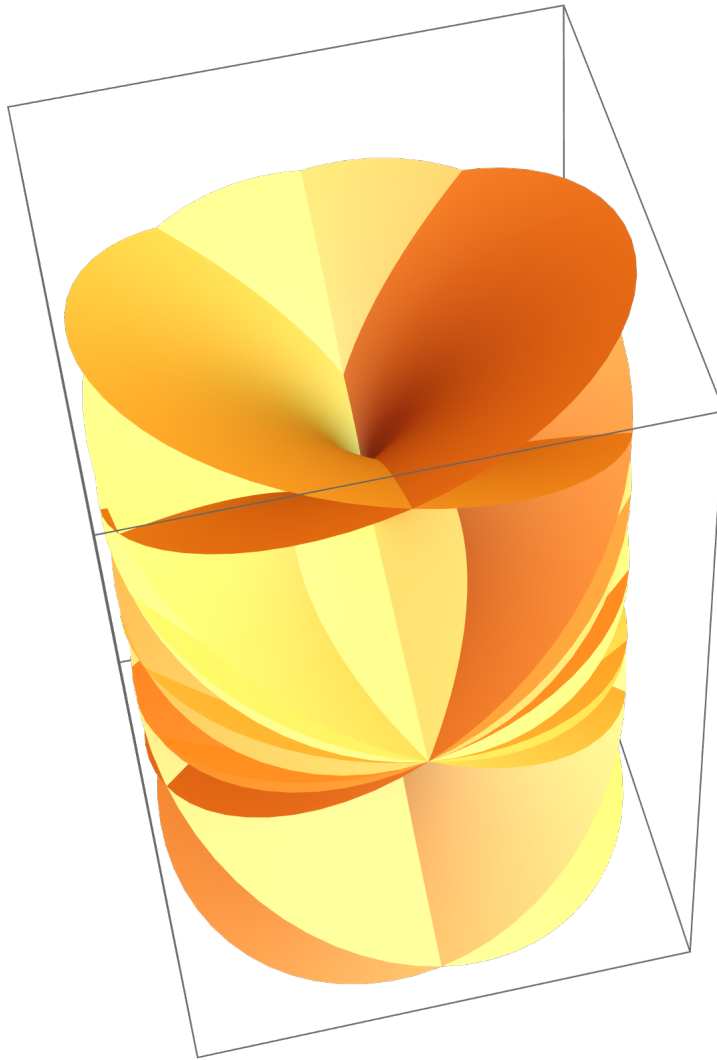


Fig. 6. Riemann Surface of $P(w)$ for $\gamma = \frac{1}{3}$.

{Velocity Inside: $f(w)$ for $\gamma = \frac{1}{3}$ }

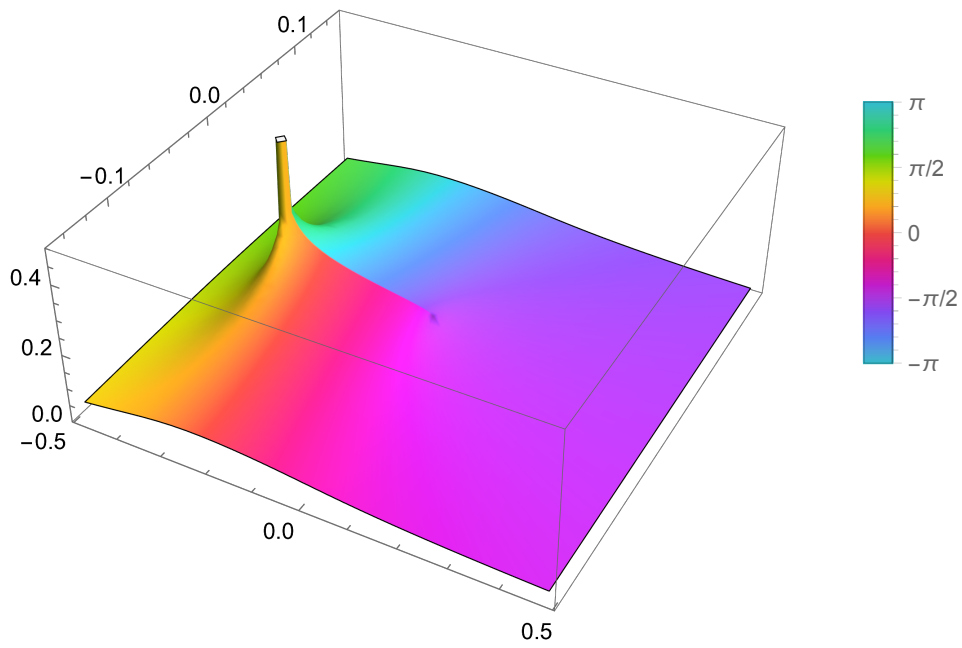


Fig. 7. The complex 3D map of $f(w)$ corresponding to complex velocity inside the loop. The color describes the phase, and the height - the amplitude of $f(w)$

{Velocity Outside: $g(w)$ for $\gamma = \frac{1}{3}$ }

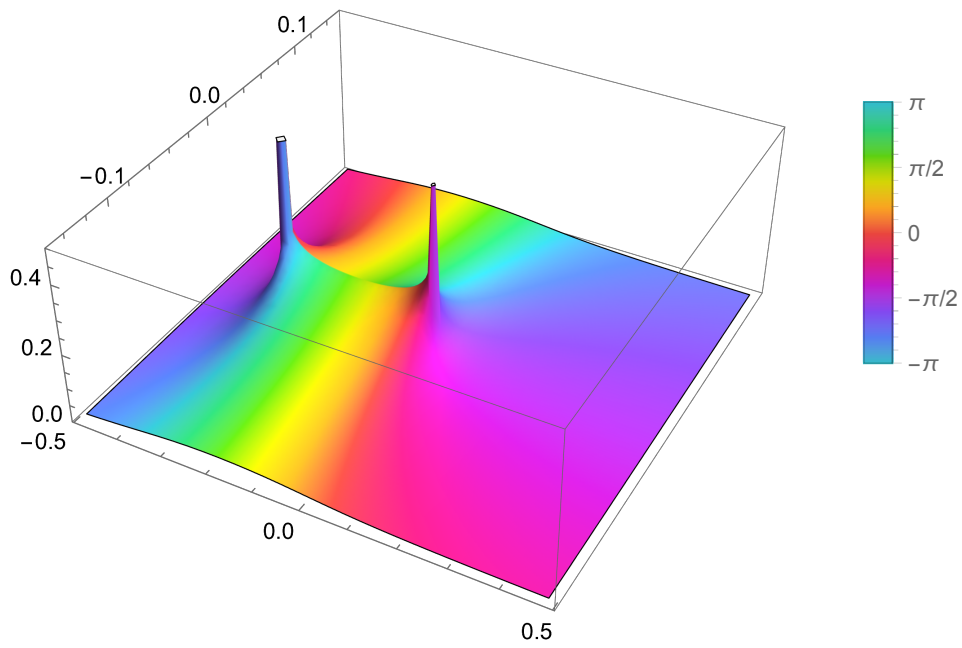


Fig. 8. The complex 3D map of $g(w)$ corresponding to complex velocity outside the loop. The color describes the phase, and the height - the amplitude of $g(w)$

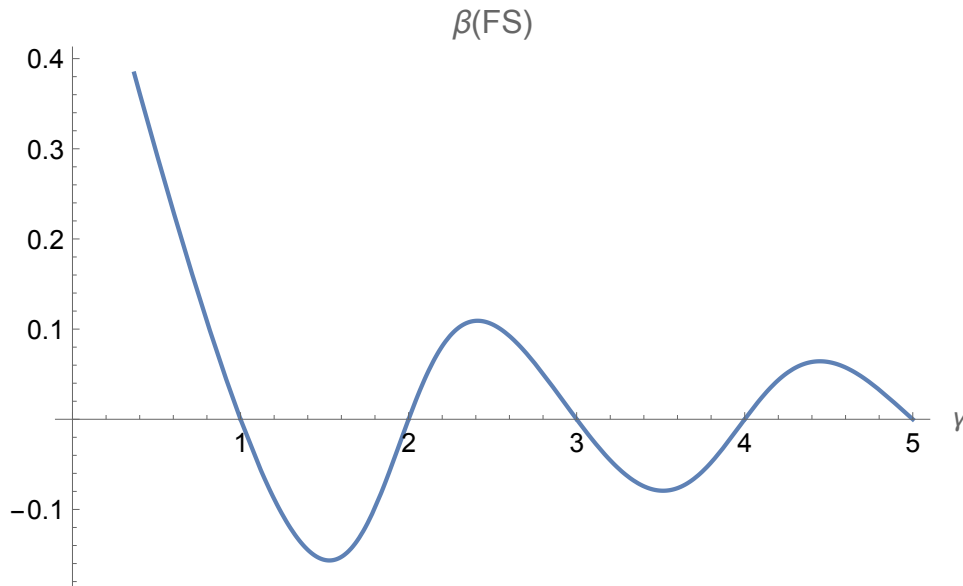


Fig. 9. The plot of the Falkner-Skan parameter β_{FS} as a function of γ . For every stability interval $\gamma \in (2k, 2k + 1)$ this parameter stays in the interval $(0, 1)$ which is sufficient for stability of the solution of the Navier-Stokes equation at the boundary layer near the corner.

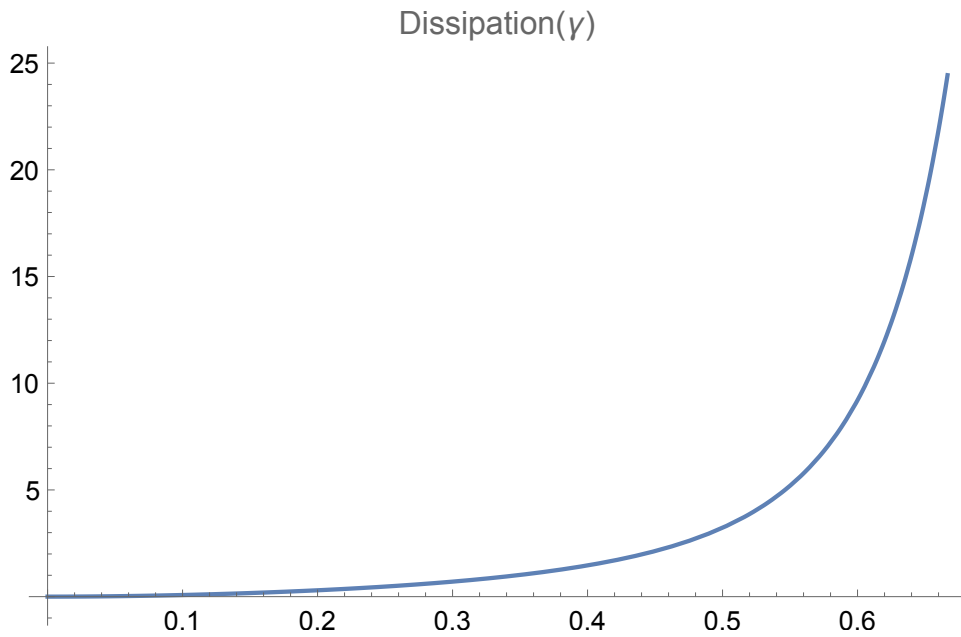
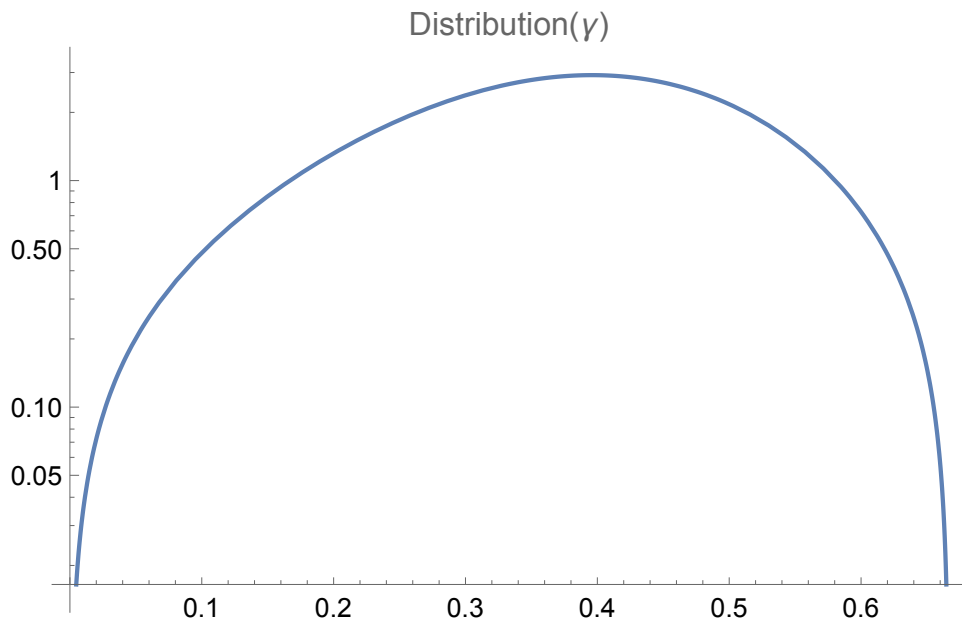
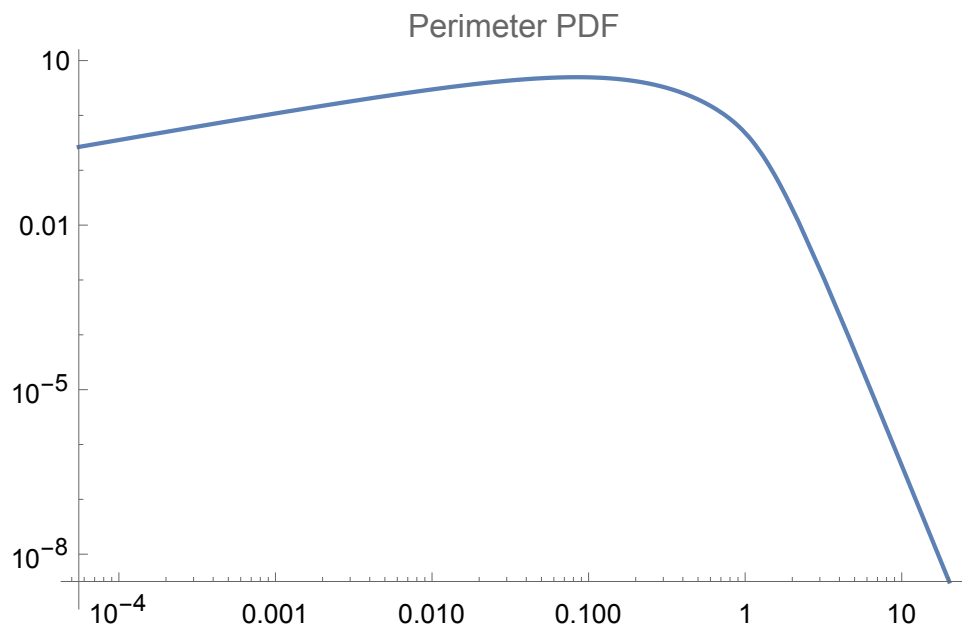


Fig. 10. The energy dissipation as a function of γ

Fig. 11. The probability distribution of γ Fig. 12. The probability distribution of perimeter $|C|$ of the cross-section

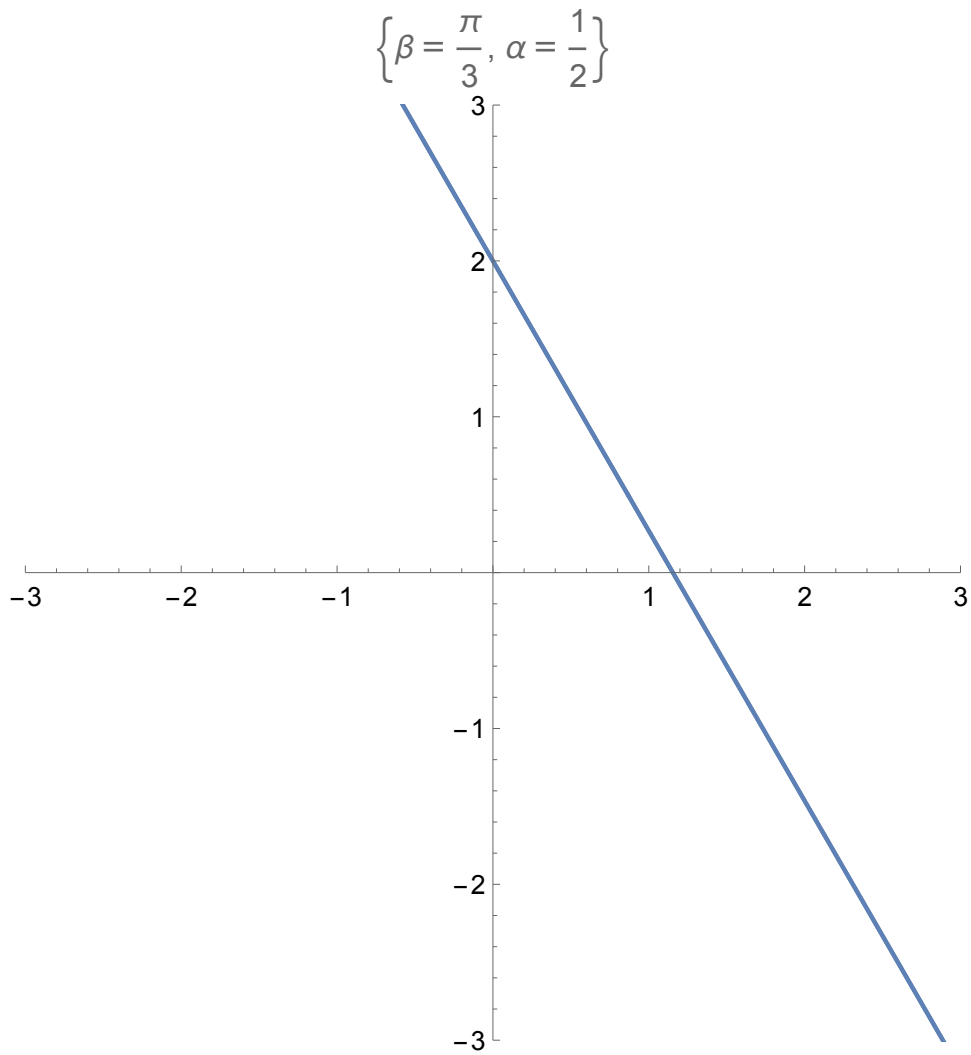
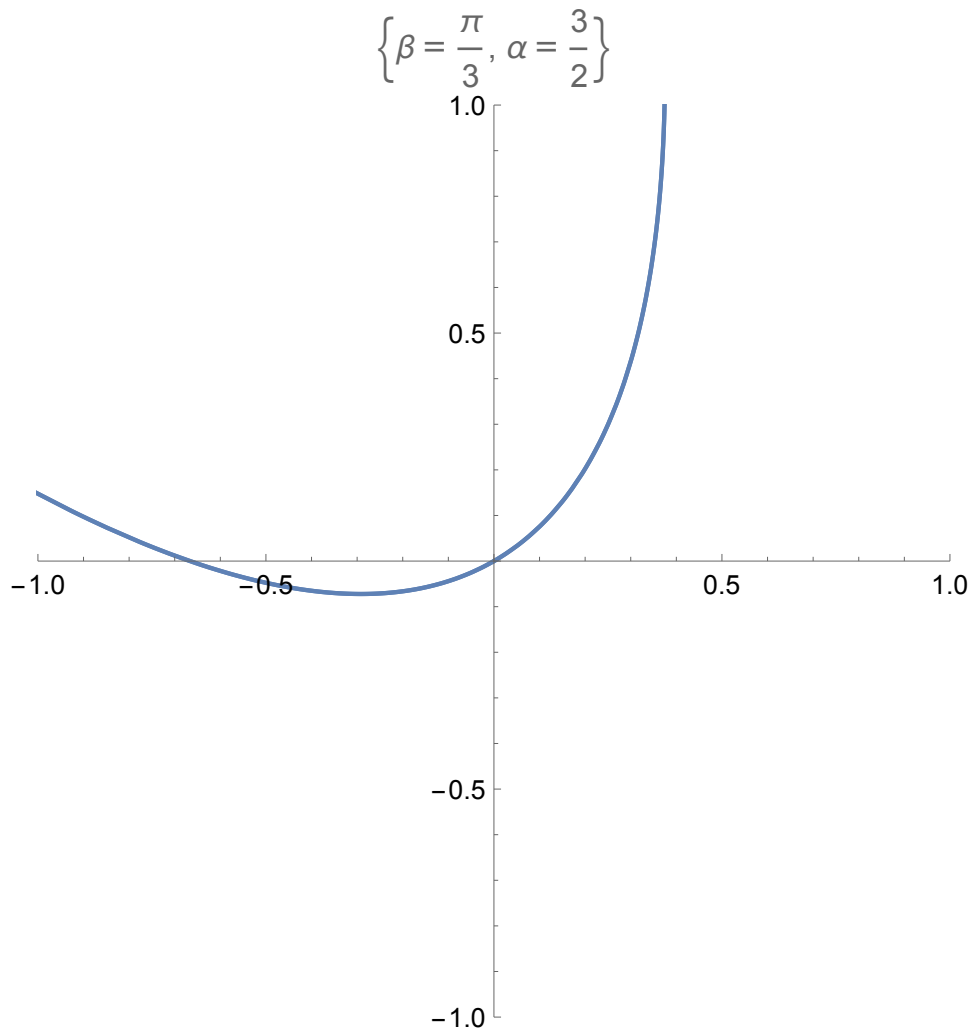
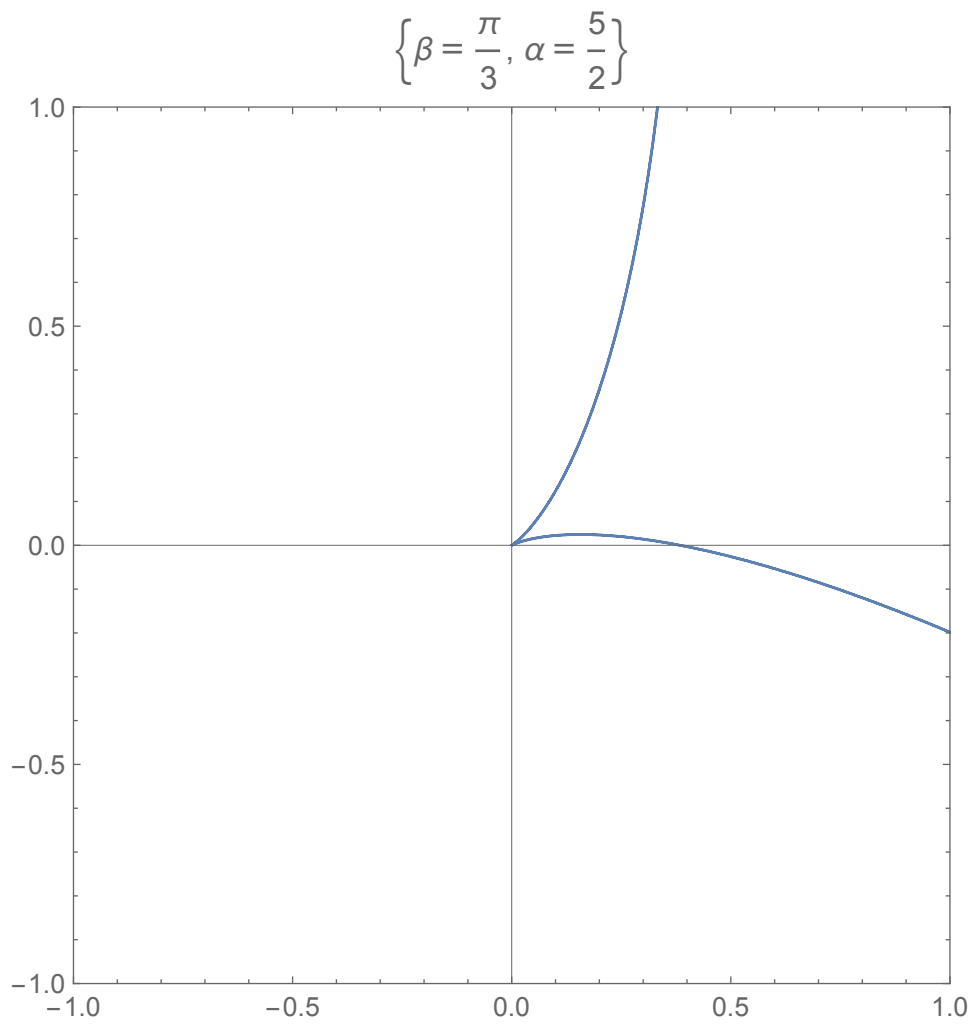
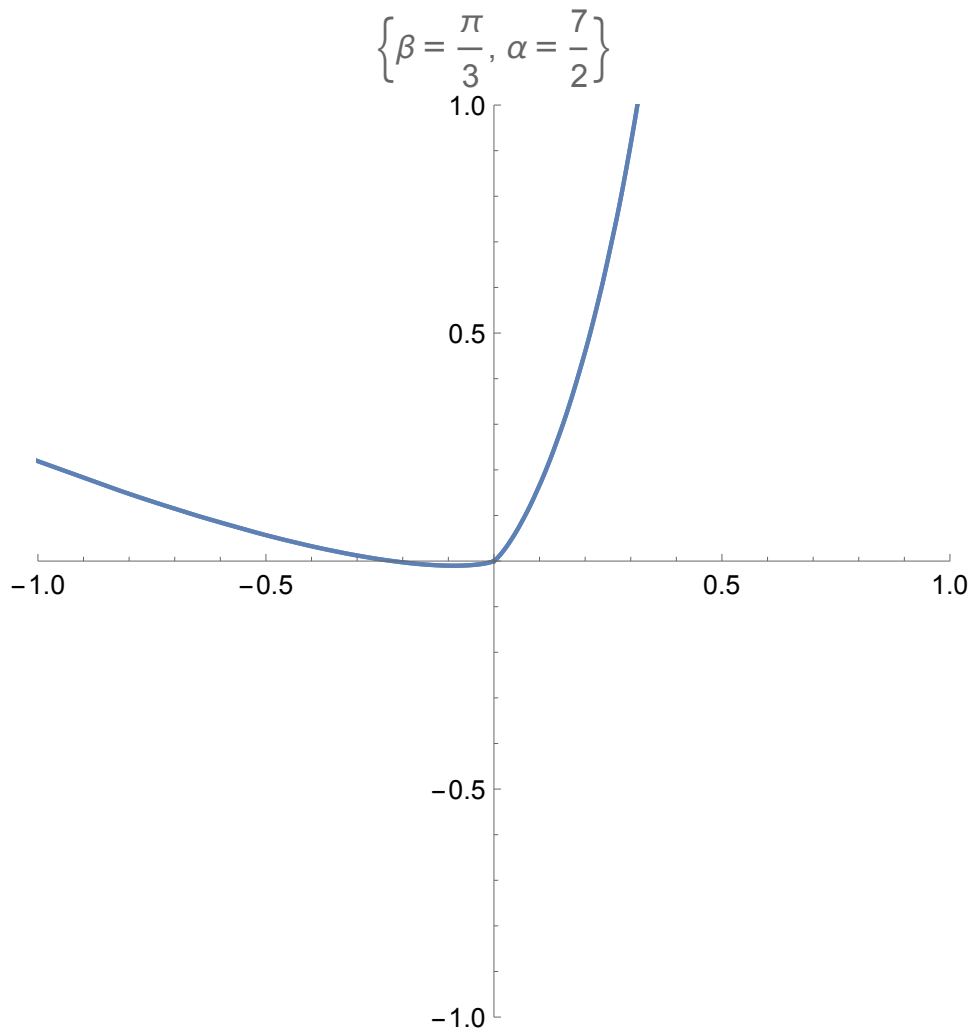


Fig. 13. The Burgers-Townsend case, $n = 0$.

Fig. 14. The CVS for $n = 1$.

Fig. 15. The CVS for $n = 2$.

Fig. 16. The CVS for $n = 3$.

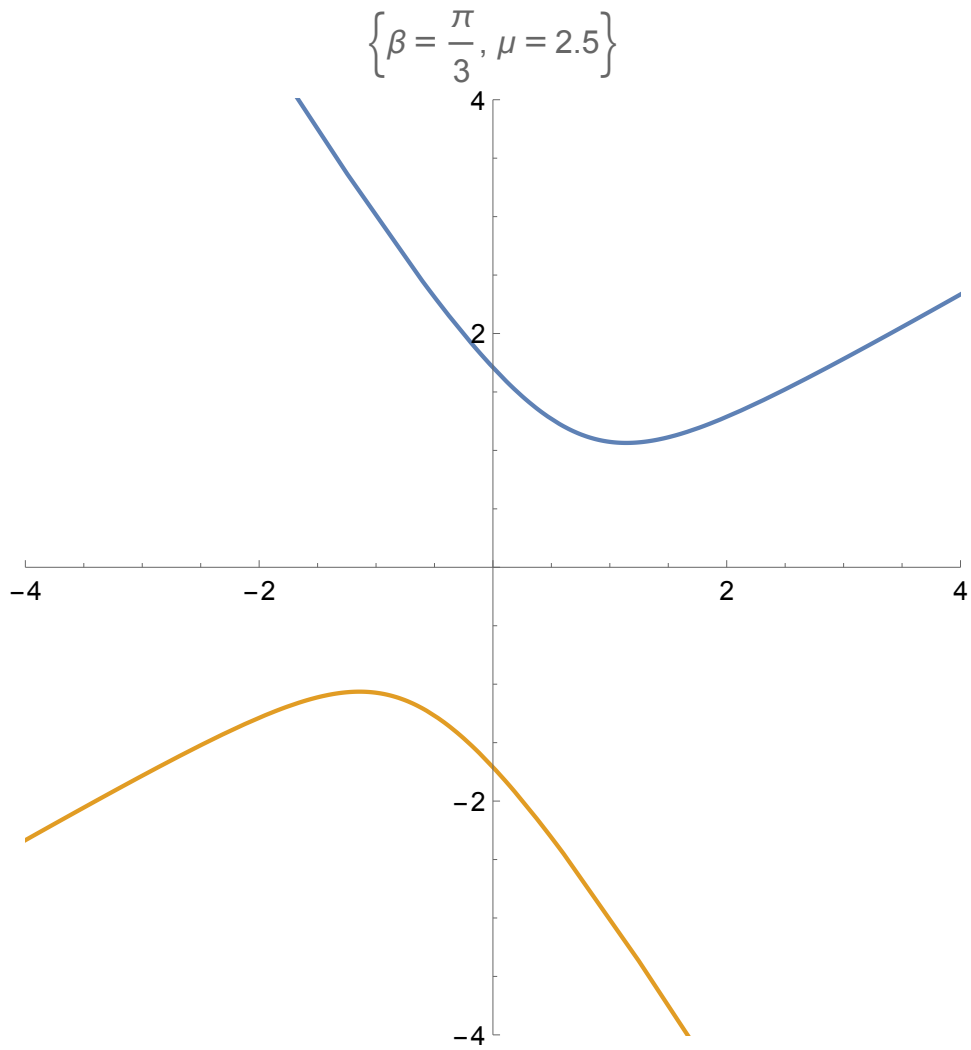


Fig. 17. The hyperbolic CVS for $\beta = \pi/3, \mu = 2.5$.

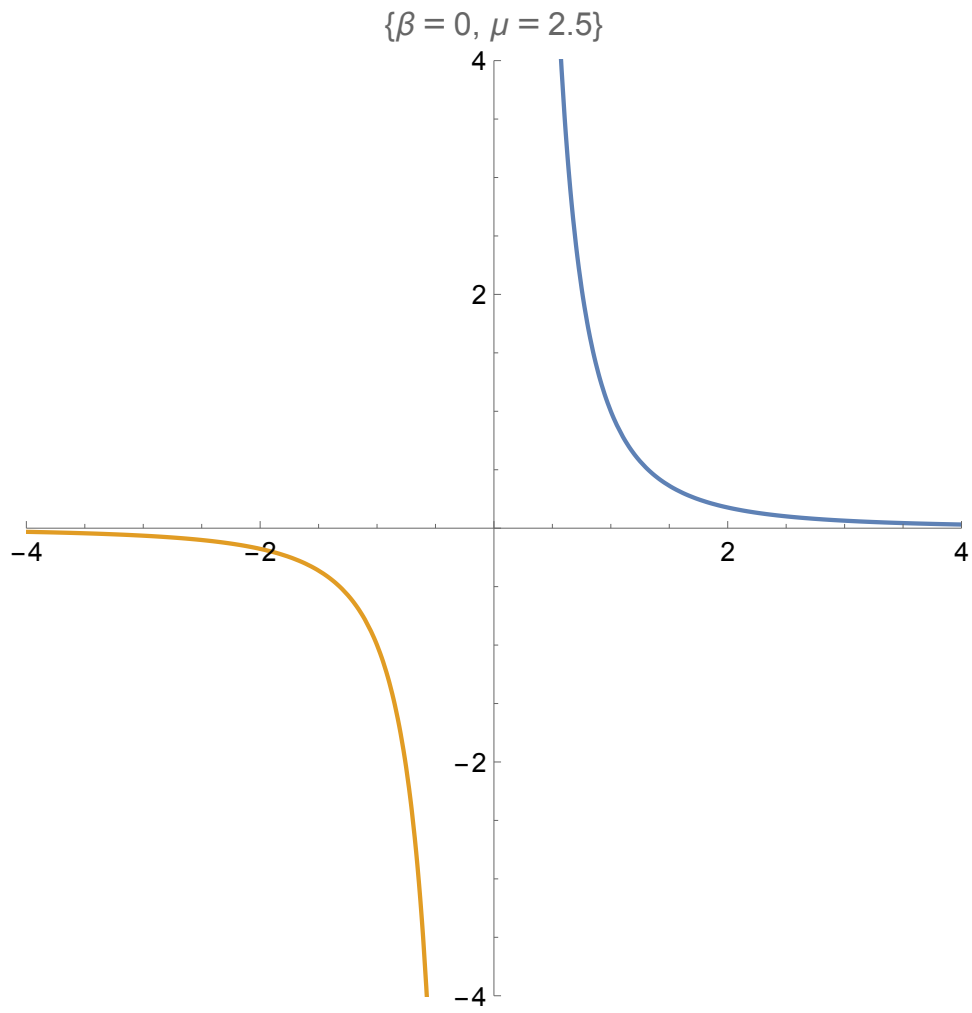


Fig. 18. The hyperbolic CVS for $\beta = 0, \mu = 2.5$

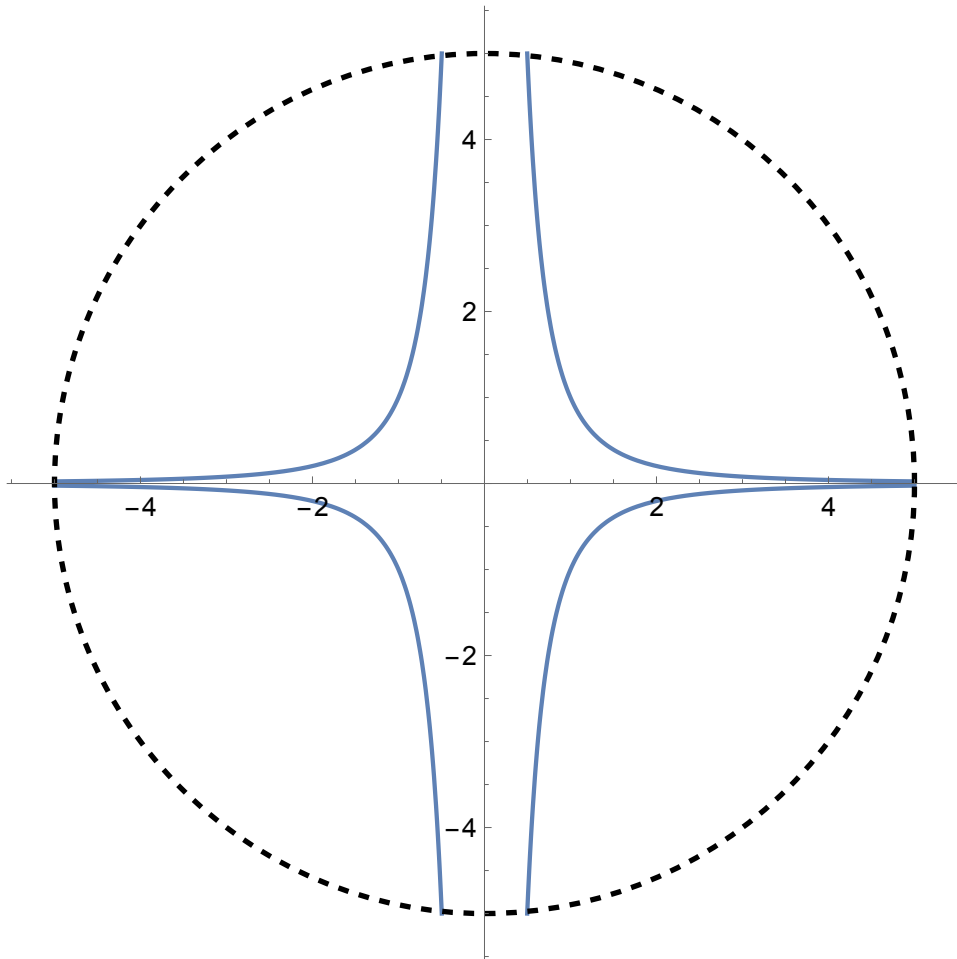


Fig. 19. The loop made of four branches of hyperbola.

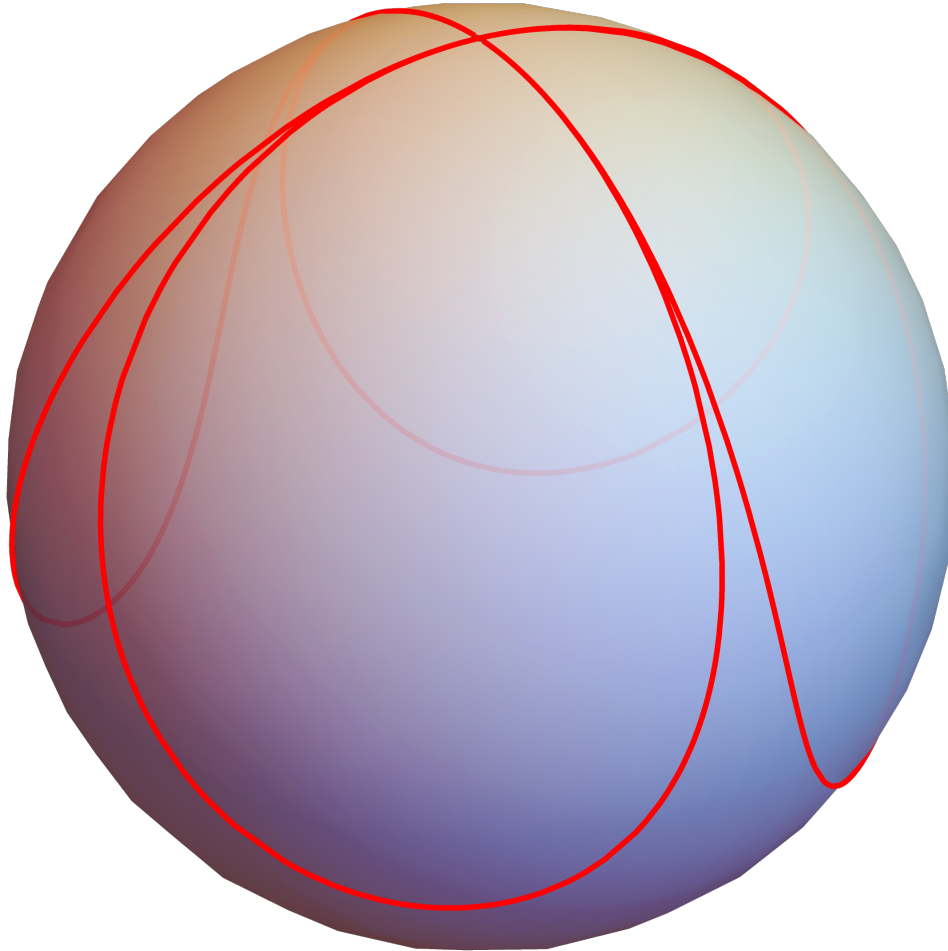


Fig. 20. The stereographic projection of four branches of hyperbola on the Riemann sphere.

$$\eta = 1 + \frac{0.+1.51i}{w^{2.51}}$$

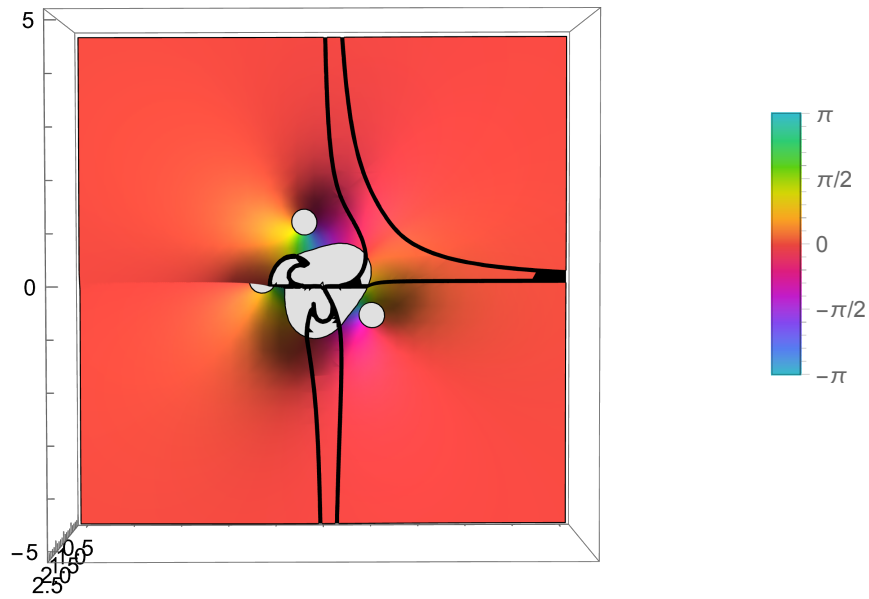


Fig. 21. The complex Map3D of the holomorphic function $\eta'(w) = 1 + i\mu w^{\mu-1}$ for $\mu = 1.51$. The height is $|\eta'|$, the color is $\arg \eta'$. The square root singularities of inverse function $\eta(w)$ is located at the points where $\eta'(w) = 0$. They are indicates as a holes on the surface (white circles). The black lines are described by $(\operatorname{Re} \eta(w))^\mu (\operatorname{Im} \eta(w))^\mu = \pm 1$. The physical region is outside the black line in the first quadrant, and there are no singularities there.

$$\eta = 1 + \frac{0. + 2.i}{w^3}$$

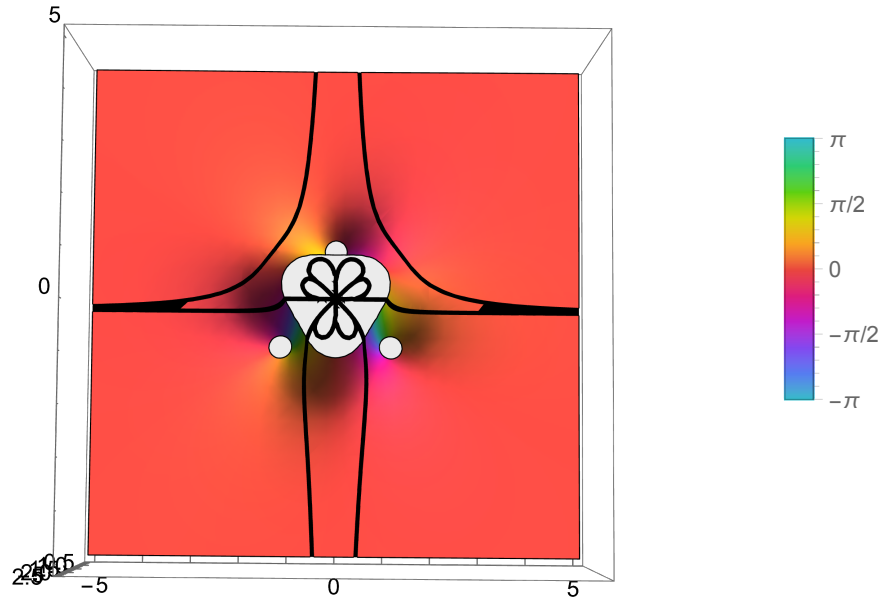


Fig. 22. The complex Map3D of the holomorphic function $\eta'(w) = 1 + i\mu w^{-\mu-1}$ for $\mu = 2$. The height is $|\eta'|$, the color is $\arg \eta'$. The square root singularities of inverse function $\eta(w)$ is located at the points where $\eta'(w) = 0$. They are indicates as a holes on the surface (white circles). The black lines are described by $(\operatorname{Re} \eta(w))^\mu \operatorname{Im} \eta(w) = \pm 1$. The physical region is outside the black line in the first quadrant, and there are no singularities there.

$$\eta = 1 + \frac{0.+2.99i}{w^{3.99}}$$

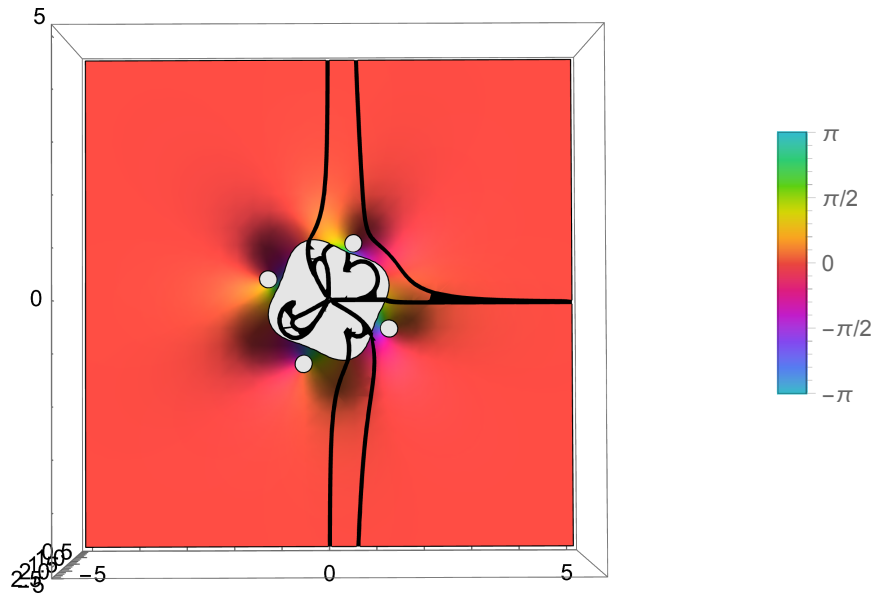


Fig. 23. The complex Map3D of the holomorphic function $\eta'(w) = 1 + i\mu w^{-\mu-1}$ for $\mu = 2.99$. The height is $|\eta'|$, the color is $\arg \eta'$. The square root singularities of inverse function $\eta(w)$ is located at the points where $\eta'(w) = 0$. They are indicates as a holes on the surface (white circles). The black lines are described by $(\operatorname{Re} \eta(w))^\mu \operatorname{Im} \eta(w) = \pm 1$. The physical region is outside the black line in the first quadrant, and there are no singularities there.

$$\{V, \mu = 1.7, v_n \leq 4.32199 \times 10^{-16}\}$$

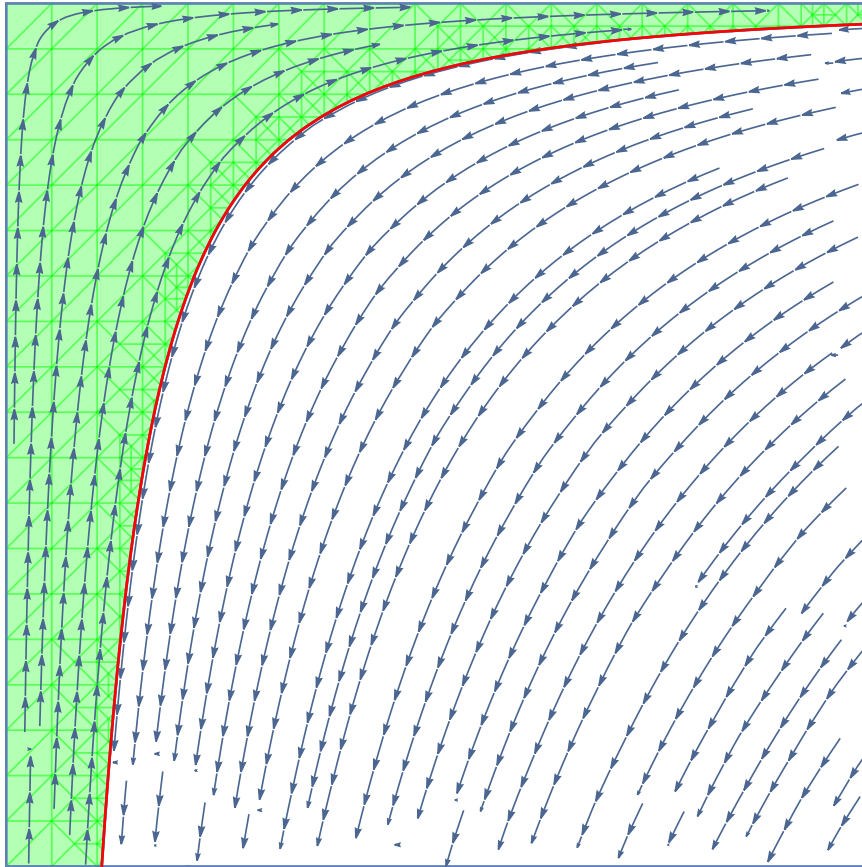


Fig. 24. The stream plot in IV quadrant of xy plane for $\mu = 1.7$. The green fluid is inside, the clear fluid is outside the vortex surface (red). The flow in other quadrants can be obtained by reflection against the x and y axes. The normal velocity vanishes at the vortex sheet on both sides, with accuracy $\sim 10^{-16}$.

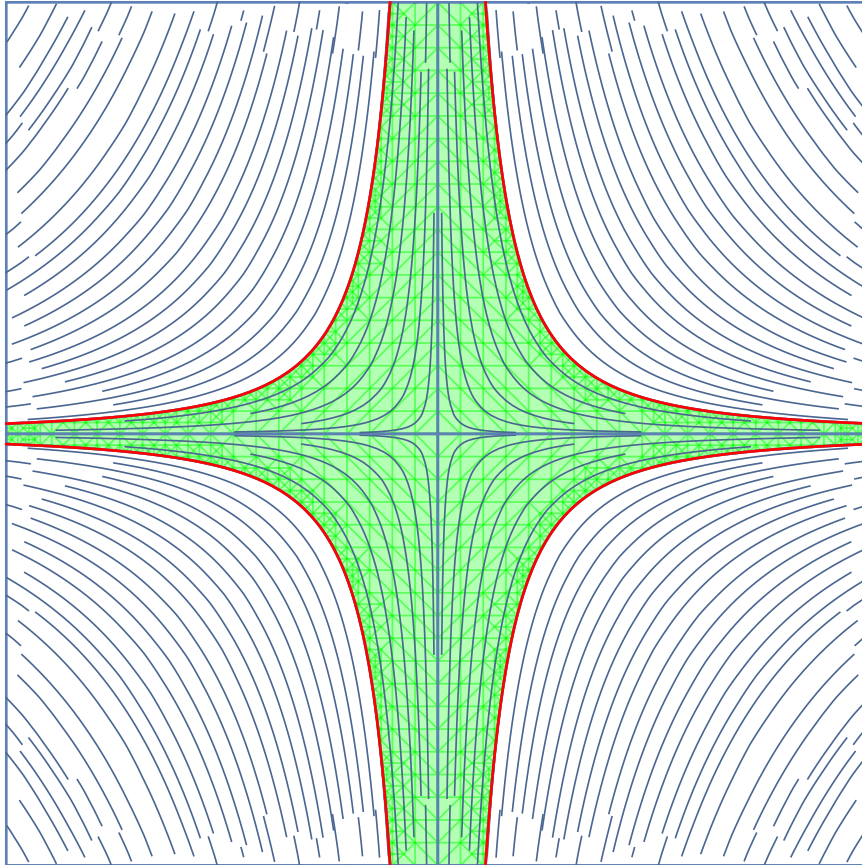


Fig. 25. The stream plot in xy plane for $\mu = 1.7$. The green fluid is inside, the clear fluid is outside the vortex surface (red)